Short-Pulse Photofragmentation and Fluorescence-based Diagnostics - Development and Applications

Jonsson, Malin

2015

Short-Pulse Photofragmentation and Fluorescence-based Diagnostics
–Development and Applications

Malin Jonsson

LUND
UNIVERSITY

Printed in Sweden by Media-Tryck, Lund University
Lund 2015

Lund Reports on Combustion Physics, LRCP-191
ISBN 978-91-7623-514-0 (print)
ISBN 978-91-7623-515-7 (pdf)
ISSN 1102-8718
ISRN LUTFD2/TFCP-191-SE

Malin Jonsson
Division of Combustion Physics
Department of Physics
Lund University
P.O Box 118, SE-211 00 Lund, Sweden

Abstract

The work presented in the thesis covers the use of laser-induced fluorescence (LIF) and photofragmentation laser-induced fluorescence (PFLIF) with short laser pulses to determine species concentrations in different combustion environments. To attain quantitative species concentrations using LIF investigations of the influence of collisional quenching on the fluorescence signal strength is of vital importance, which can be done by measuring the fluorescence lifetime. A method for simultaneous measurements of fluorescence lifetimes of two species, present along a line, is described and discussed. The experimental setup is based on picosecond laser pulses tuned to excite two different species, whose fluorescence signals are detected with a streak camera. The concept is demonstrated for fluorescence lifetime measurements of CO and OH in laminar methane/air flames. The measured one-dimensional lifetime profiles generally agree well with lifetimes calculated from quenching cross sections found in literature and quencher concentrations predicted by the GRI 3.0 chemical mechanism. DIME, dual imaging with model evaluation, a method enabling fluorescence lifetime imaging of toluene is shortly discussed.

The second technique, i.e. PFLIF, is used to study H_2O_2 and HO_2, which both are molecules lacking accessible bound electronically excited states. Here, a pump laser pulse of 266 nm dissociates the molecules into OH fragments, which after a short time delay (nanosecond time scale), are probed with LIF using a second laser pulse tuned to an OH absorption line. The technique is investigated based on both nanosecond and picosecond pulses, in which the picosecond pulses offer the possibility to study the dissociation process in great detail. In the work presented, PFLIF is for the first time used for two-dimensional imaging of HO_2 in laminar flames and for quantitative imaging of H_2O_2 in a homogenous charged compression (HCCI) engine. In methane/air flames an interfering OH signal contribution is observed in the product zone and found to originate from photolysis of hot CO_2, whereas an interfering OH signal contribution is observed in the reaction zone arising from free oxygen atoms formed when HO_2 is photodissociated and reacting with CH_4 and/or H_2O. In the HCCI experiments, one- and two-dimensional quantitative H_2O_2 concentrations at different piston positions are extracted via an on-line calibration procedure. In terms of mass fraction levels, the crank-angle resolved experimental data agree well with simulated H_2O_2 mass fractions. The minor deviations are mainly due to signal interference from HO_2 not accounted for in the experiments, and inhomogeneities in the H_2O_2 spatial distributions not predicted by the models. Finally, PFLIF is employed for OH thermometry in different reacting flows,

including the HCCI engine. The method creates OH molecules at a lower temperature range than where they naturally occur, i.e. providing OH thermometry at lower temperatures. In this temperature regime the technique also becomes more sensitive since the rotational population distribution has a stronger temperature dependence.

Populärvetenskaplig sammanfattning

Eld har fascinerat människan i alla tider. Att sitta och värma sig vid en lägereld, sjunga sånger eller bara titta på hur elden rör sig är något de flesta har upplevt. Hur många har egentligen funderat på var värmen kommer ifrån, hur den gula färgen uppstår eller vad eld egentligen består av? Några av frågorna finns det nu svar på, men fortfarande finns det mycket att utforska.

De flesta håller nog med om att förbränning är något människan har sysslat med sedan urminnes tider, till exempel för matlagning och uppvärmning, och snart borde tillhöra historien. Så är dock ingalunda fallet. Idag kommer mer parten av all energiproduktion i världen från förbränning av fossila bränslen. Det verkar därmed troligt att vi kommer fortsätta utnyttja förbränning ett bra tag framöver. Det är därför viktigt att förstå olika förbränningsprocesser, för att minska bränsleförbrukningen, partikel-utsläppen och minimera miljöpåverkan. Förbränning är väldigt komplicerat och innefattar i allmänhet tusentals reaktioner mellan hundratals olika ämnen. De kemiska reaktionerna sker mycket snabbt och är starkt beroende av tryck, temperatur och koncentrationen av ämnen i den närliggande miljön.

Laser-baserade tekniker erbjuder möjligheten att studera kaotiska (turbulenta) flöden, kemiska och fysikaliska reaktioner, men även mätningar av temperaturer och ämneskoncentrationer. Laserljus besitter egenskaper som gör det möjligt att mäta på långa avstånd och i miljöer där det är svårt att komma åt sitt mätobjekt. En annan viktig fördel är att när laserljuset passerar genom till exempel en eld störs inte de kemiska reaktionerna som kontinuerligt äger rum. Mätningarna blir därmed beröringsfria samtidigt som man mäter i objektets naturliga miljö. Slutligen, lasern ger möjligheten att samla in detaljerad information om hur ämneskoncentrationer är fördelade i två dimensioner och hur de ändrar sig i tiden.

Den vanligaste tekniken som används inom förbränning heter laser-inducerad fluorescens (LIF). Tekniken bygger på att man belyser den molekyl man är intresserad av med laserljus innehavande en specifik färg. Molekylen kommer att absorbera ljuset och därmed energin, vilket leder till att molekylen hamnar i ett högre energitillstånd. Detta kan liknas vid att man får energi så att man kan ta sig upp ett steg i en trappa. Varje molekyl som lasern lyft upp ett trappsteg har möjligheten att sända ut en fluorescensfoton (ljus) när den faller tillbaka till det lägsta trappsteget (grundtillståndet). Olika molekyler har olika avstånd mellan trappstegen, vilket innebär att man med olika energi på ljuset, dvs. olika färg, kan nå till olika trappsteg och därmed studera enskilda molekyler. I den bästa av världar betyder det att man genom att mäta antalet fluorescensfotoner kan bestämma antalet molekyler. Tyvärr är

verkligheten en annan. Mer än 99 procent (typiskt vid normalt tryck) av molekylerna på det övre trappsteget sänder inte ut ljus. Istället förlorar molekylerna sin överskottsenergi genom kollisioner med sina grannar. Intensiteten på fluorescensljuset ger därför inte information om det exakta antalet molekyler. Istället måste man ta reda på hur kollisionerna påverkar fluorescensljuset. Om det är många kollisioner kommer fluorescensljuset vara kortlivat, medan det blir långlivat om kollisionerna är få. I detta arbete har längden på fluorescensljuset studerats i olika förbränningssituationer, t.ex. en flamma och ett gas flöde. När ett mått på kollisionernas inverkan är bestämt kan mätdata korrigeras och man är ett stort steg närmare målet att bestämma en absolut ämneskoncentration.

Laser-inducerad fluorescens bygger på att trappstegen hos molekylerna består av hela trappsteg. Det finns molekyler där de högre energinivåerna är som rutschkanor istället för trappsteg. Detta leder till att när man sänder in laserljus på molekylen så kommer den ”glida av” trappsteget, vilket innebär att molekylen kommer sönderdelas (dissocieras) istället för att skicka ut ljus. I detta arbete beskrivs hur man kan studera dessa molekyler med en teknik som heter fotofragmentation laser-inducerad fluorescens. Tekniken har använts för att mäta ämneskoncentrationen av väteperoxid (H_2O_2) och hydroperoxyl (HO_2) i verkliga förbränningssituationer, t.ex. i en motor och i en flamma.

Möjligheten att mäta ämneskoncentrationer är en viktig pusselbit för förståelsen av moderna förbränningsprocesser. En ökad kunskap är avgörande för till exempel utvecklingen av effektivare och miljövänligare motorkoncept. Målet är att ytterligare minska bränsleförbrukningen och utsläppen av farliga ämnen och partiklar i vår luft. För en bättre miljö, inte bara för oss utan även för framtida generationer.

List of papers

I. M. Jonsson, A. Ehn, M. Christensen, M. Aldén, J. Bood. *Simultaneous one-dimensional fluorescence lifetime measurements of OH and CO in premixed flames*, Applied Physics B, 115(1), 35-43, 2014

II. A. Ehn, M. Jonsson, O. Johansson, M. Aldén, J. Bood. *Quantitative oxygen concentration imaging in toluene atmospheres using Dual Imaging with Modeling Evaluation*, Experiments in Fluids, 54(1), 1-8, 2013

III. M. Jonsson, J. Borggren, M. Aldén, J. Bood. *Time-resolved spectroscopic study of photofragment fluorescence in methane/air mixtures and its diagnostic implications*, Applied Physics B, 120(4), 587-599, 2015

IV. O. Johansson, J. Bood, B. Li, A. Ehn, Z.S. Li, Z.W. Sun, M. Jonsson, A.A. Konnov, M. Aldén. *Photofragmentation laser-induced fluorescence imaging in premixed flames*, Combustion and Flame, 158(10), 1908-1919, 2011

V. M. Jonsson, K. Larsson, J. Borggren, M. Aldén, J. Bood. *Investigation of photochemical effects in flame diagnostics with picosecond photofragmentation laser-induced fluorescence*, Submitted to Combustion and Flame, 2015

VI. K. Larsson, M. Jonsson, J. Borggren, E. Kristensson, A. Ehn, M. Aldén, J. Bood. *Single-shot photofragment imaging by structured illumination*, Accepted, Optics Letters, 2015

VII. B. Li, M. Jonsson, M. Algotsson, J. Bood, Z.S. Li, O. Johansson, M. Aldén, M. Tunér, B. Johansson. *Quantitative detection of hydrogen peroxide in an HCCI engine using photofragmentation laser-induced fluorescence*, Proceedings of the Combustion Institute, 34(2), 3573-3581, 2013

VIII. G. Coskun, M. Jonsson, J. Bood, M. Tunér, M. Algotsson, B. Li, Z.S. Li, H.S. Soyhan, M. Aldén, B. Johansson. *Analysis of in-cylinder H_2O_2 and HO_2 distributions in an HCCI engine – Comparison of laser-diagnostic results with CFD and SRM simulations*, Combustion and Flame, 162(9), 3131-3139, 2015

IX. E. Malmqvist, M. Jonsson, K. Larsson, M. Aldén, J. Bood. *Two-dimensional OH-thermometry in different reacting flows using photofragmentation laser-induced fluorescence*, Submitted to Combustion and Flame, 2015

Related work

X. B. Kaldvee, J. Wahlqvist, M. Jonsson, C. Brackmann, B. Andersson, P. van Hees, J. Bood, M. Aldén. *Room fire characterization using highly range resolved picosecond lidar diagnostics and CFD simulations,* Combustion Science and Technology, 185(5), 749-765, 2013

XI. A. Ehn, M. Levenius, M. Jonsson, M. Aldén, J. Bood. *Temporal filtering with fast ICCD cameras in Raman studies*, Journal of Raman Spectroscopy, 44(4), 622-629, 2013

Contents

1 Introduction

Combustion of fossil fuels is the major source of energy production in today's society [1]. It is known that the emissions it has resulted in during the last century have had a profound impact upon both the global and the local climate. It has increased the global temperature which in turn, has led to a reduction in the snow and ice coverage, to higher sea levels and to the more frequent occurrence of extreme weather conditions [2]. In addition to its environmental effects, it has also had negative effects on health, particularly in densely populated cities, where smog and presence of particles in the air have led to asthma and lung cancer, for example [3].

The processes combustion involves are complex characterized by complicated chemistry, involving typically hundreds of reactions and hundreds of species, often in turbulent flow fields with large temperature and pressure gradients. Having detailed information on the intermediate trace species and temperatures involved is thus of vital importance for being able to understand the combustion processes and pollutant formation associated with them. On the basic of such knowledge, chemical kinetics and fluid mechanical models can be developed, which are able to describe combustion systems in detail, leading to improvements in existing combustion systems as well as to the development of new and better technologies. The ability to detect species non-intrusively and to measure the temperatures involved in combustion through use of laser-diagnostic techniques has had a profound impact on combustion research during the last 30 years [4, 5]. Laser-based techniques provide the possibility of probing temperatures, turbulent flow fields and species concentrations with a high degree of spatial resolution through the laser beam being formed into a thin laser sheet and sensitive cameras being employed. A high temporal resolution is achieved here through the use of short laser pulses with a duration ranging from nanoseconds to femtoseconds.

However, despite the extensive development of a large variety of laser-based techniques, quantitative data are still very difficult to obtain, especially when the methods in question are employed in practical combustion devices. Laser-induced fluorescence (LIF) is probably the most commonly used technique for measuring the relative concentrations of minor species in combustion environments, due to its high sensitivity, high temporal and spatial resolution, and its ability to deliver two-dimensional images of the trace species. The fluorescence signal strength generated is related, however, not only to the concentration of the excited species, but is also strongly dependent upon non-radiative relaxation processes, primarily those of collisional quenching. Quenching, i.e. deactivation of the excited molecule through

molecular collisions, is dependent upon the collisional partner, i.e. on the chemical composition, pressure, temperature, and quantum state of the molecules. The use of short laser pulses together with a detector with the capacity to resolve the temporal development of the fluorescence signal opens up the possibility of measuring the fluorescence lifetime, which is directly related to the collisional quenching.

Laser-induced fluorescence relies on the ability to excite molecules from a ground state to a higher electronic energy state. Several of the molecules involved in combustion chemistry possess unbound electronically excited states such that after UV excitation they dissociate into fragments instead of emitting fluorescence. Through probing the fragments with LIF, indirect detection of the precursor molecule is possible, since the fluorescence intensity that is induced is related to the concentration of the parent species. This technique is called photofragmentation laser-induced fluorescence (PFLIF). Although it provides a possibility of measuring non-fluorescing species indirectly, due to its non-species-specific nature, it has certain limitations. Depending upon the application involved, there can be potential problems related to signal interference due to naturally existing fragment species, signal interference from other species that generate the same fragments, as well as photochemical interference signals. It is possible to make the technique more species-specific by conducting fundamental studies of the photofragmentation process and performing time-resolved measurements on the fragments. This leads to knowledge of the initial population of the fragments, the intermolecular systems that are present, as well as information of the chemical kinetic processes involved.

1.1 Motivation

The papers taken up and discussed in the thesis can be divided into three separate but related parts. The first part concerns the topic of how to achieve quantitative species concentrations in combustion systems by utilizing picosecond LIF (Papers I-II). In the work presented in Paper I, the fluorescence lifetime of two different species is measured simultaneously by use of two tunable picosecond laser pulses with the aim of determining dual quantitative species concentrations. Paper II demonstrates the Dual Imaging with Modeling Evaluation (DIME) approach and how it can be used to obtain quantitative oxygen concentration images. The second part (Papers III-VI) discusses and demonstrates the first applications of PFLIF for two-dimensional imaging of hydrogen peroxides (H_2O_2 and HO_2) in premixed laminar flames. In the work described in Paper IV this technique is based on nanosecond laser pulses and the signal interference produced by other species in the product zone are being discussed. Paper V presents what is the first combination thus far of PFLIF and picosecond laser pulses for the detection of hydrogen peroxides in flames, the potential chemically induced signal interference from the reaction zone are also being discussed. In the work presented in Paper VI, PFLIF is for the first time combined with structured

illumination for examining possibilities of achieving in this way single-shot imaging of non-fluorescing species in flames. The dissociation process in methane/air mixtures (Paper III) and in laminar flames is also discussed. Finally, in the last part of the thesis (Papers VII-IX), the successful use of PFLIF for one- and two-dimensional quantitative H_2O_2 concentration measurements in an HCCI engine via a calibration procedure is demonstrated. The averaged in-cylinder two-dimensional temperature distribution can also be measured by PFLIF by recording OH-fragment excitation spectra.

The overall focus of the thesis is on two questions; first how quantitative species concentrations in combustion applications can be achieved, and secondly how PFLIF can be used, and with which limitations, in practical combustion applications. In Chapter 2, the basic theories connected with use of picosecond LIF and PFLIF are presented. The results pertaining to Papers I-II and related discussions are presented in Chapter 3. The dissociation process induced in methane gas and hydrocarbon flames by a 266-nm pulse is discussed in Chapter 4. Chapter 5 reviews the application of PFLIF to methane/air flames subjected to nanosecond and picosecond excitation. The major results obtained in applying PFLIF to an HCCI engine are taken up in Chapter 6. The thesis ends with Chapter 7, in which the results obtained are summarized and conclusions are drawn, various future perspectives regarding the conducted work are being examined.

2 Measurement techniques

2.1 Laser-induced fluorescence

Fluorescence is a light-matter interaction process, described quite simply as taking place between two quantum states. Through absorption of a photon of suitable energy, a higher energy level becomes populated, followed by spontaneous light emission. Several processes can take place following absorption, as shown in the energy level diagram of OH presented in Figure 1. The dashed lines represent the radiative processes, where W specifies photoionization and A spontaneous emission, i.e. fluorescence, b_{12} and b_{21} symbolizing absorption and stimulated emission, respectively. The last two terms are related to B, the Einstein coefficient for absorption and stimulated emission, through the relationship, $b=(BI_v)/c$, where I_v is the laser intensity and c the speed of light. The solid lines represent the radiationless processes, Q being collisional quenching, P predissociation, and rotational and vibrational energy transfers being denoted as RET and VET, respectively. Fluorescence emission can take place either through a single quantum state causing a narrowband emission to take place or through several states resulting in a broadband emission. For small molecules, emission occurring between two electronic states is often in the visible or UV regime [4, 6, 7].

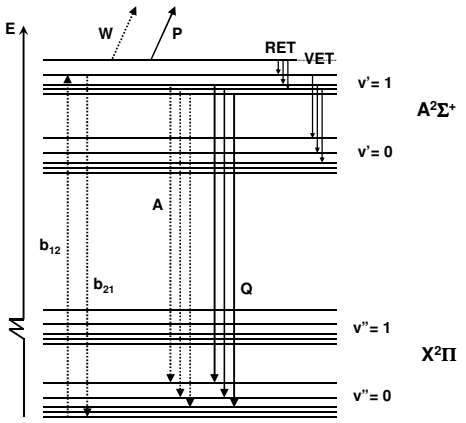

Figure 1 A schematic energy level diagram of different possible transition processes between the ground state ($X^2\Pi$) and the first excited state ($A^2\Sigma^+$) of OH. The nonradiative transitions are shown by solid lines, whereas the radiative processes are denoted by dashed lines.

The fluorescence signal induced can be described in many different ways, as defined by differing assumptions concerning the molecular system involved. If a laser pulse is used as the excitation source, the process is referred to as laser-induced fluorescence (LIF). If the system is assumed to be a two-level system, such that the entire emission is integrated over time and arises between the upper level and the ground level, the fluorescence signal S_{LIF} is given by [4, 8]

$$S_{LIF} = n_2 A \tau_{eff} V \frac{\Omega}{4\pi} \varepsilon \eta \quad . \tag{1}$$

Here n_2 is the number density of molecules in the upper level that are reached through absorption of the laser irradiance, A is the Einstein spontaneous emission coefficient between the upper and the lower level, τ_{eff} is the effective fluorescence lifetime, which depends upon the rates of quenching, of photoionization and of predissociation. V is the volume which is probed, as defined by A_{cross}, the laser beam cross-section and l, the path length, observed by the collection optics, where $V=A_{cross}l$. The last part of Equation 1 concerns the collection efficiency of the optics and the detector, where $\Omega/4\pi$ is the fraction of the solid angle which is observed, ε is the efficiency of the collection optics, and η is the responsivity of the detection system.

2.1.1 Quantitative laser-induced fluorescence

As can be clearly seen in Equation 1, many parameters need to be evaluated in order to determine the absolute molecular concentrations with use of laser-induced fluorescence. Within the area of laser-based combustion diagnostics there are several different approaches that can be taken in order to obtain quantitative species information with LIF. In many molecules that are under atmospheric pressure, high temperature, and low laser pulse energy, collisional quenching is often the dominant depletion process occurring in the upper-energy-state population.

The processes that are collision-induced can be kept to a minimum through use of a very high laser intensity, so as to obtain a saturated condition in the upper energy state of the molecule. The technique in question is termed saturated LIF. When the laser pulse energy is high, a significant portion of the population involved is pumped out of the ground level, that process together with stimulated emission that occurs in the upper state will dominate [9]. An advantage of this technique is that saturation in the upper state also tends to maximize the fluorescence signal intensity. In practice, however, it is difficult technically to generate a sufficiently high level of laser pulse energy for full saturation to be achieved since the spatial, temporal and spectral shape of a laser pulse is non-homogenous, and it is difficult to achieve full saturation in the wings of a laser pulse. Collisional quenching can also be reduced by using predissociative LIF. Here, a predissociative state is reached when absorption has

occurred and predissociation will become the dominant process in the upper level [10, 11]. The major disadvantage of this technique is the low degree of fluorescence efficiency it possesses. Hence, the ratio of the spontaneous emission to predissociation that occurs is small, resulting in low fluorescence signal strength. Collisional losses can be minimized through measurements being conducted under conditions well below atmospheric pressure [8]. Since, as mentioned earlier, collisional quenching is strongly dependent upon the pressure, and at low pressure its impact on the fluorescence signal is therefore reduced. It is difficult to employ such an approach in practical combustion situations, however, since these usually take place at pressures above atmospheric pressure.

In addition to the importance of determining the impact of collisional quenching on the LIF signal, it is also important to determine the parameters in Equation 1 that relate to the optical detection system, i.e. $V \cdot (\Omega/4\pi) \cdot \varepsilon\eta$. A method commonly employed is to calibrate against Raman or Rayleigh scattering to determine the experimental optical and detector collection factors involved [8, 12]. Another approach is to perform calibration measurements under conditions of the molecular concentration being known. The LIF signal can also be calibrated against signals obtained with use of absorption-based techniques [7]. Absorption spectroscopy is relatively straightforward, since the molecular concentration can be deduced from the Beer-Lambert law [6]. The concentration is measured there by studying the laser intensity both before and after molecular absorption under conditions of known path length. Major drawbacks of this technique are that a relatively high molecular concentration is required and that the technique is a line-of-sight method, which means that average concentrations are measured (if the temperature is constant throughout the sample as a whole). Intra-cavity laser absorption spectroscopy (ICLAS) and cavity-ring-down spectroscopy (CRDS) are two absorption-based techniques that enable extremely low species concentrations to be detected [13, 14]. Unfortunately, both techniques are relatively new in terms of their application to combustion situations and the setups involved are rather complicated as compared with a LIF-setup [13].

Nevertheless, even if one of the above-described approaches is used, knowledge is needed concerning the laser pulse energy and spectral bandwidth, the temperature, the Einstein absorption and emission coefficients, and the quenching losses involved in order for absolute molecular concentrations to be determined with LIF. Since under conditions of atmospheric pressure, high temperatures, and low laser intensity, collisional quenching is responsible for most of the LIF-signal losses that occur, it is thus highly advantageous if the value of the quenching can be determined.

2.1.2 Collisional quenching

Collisional quenching, Q, is often the mechanism primarily responsible for radiationless deexcitation, meaning that only a minor fraction of the excited molecules contributes to the fluorescence signal [4]. Such quenching is strongly affected by the surrounding temperature, the molecular composition at hand and the pressure. In a real combustion system, in which there is usually a wide range of both temperatures and pressures, collisional quenching has a major effect on the fluorescence signal produced. The quenching effects can be measured experimentally by use of a laser pulse appreciably shorter in duration than the anticipated fluorescence lifetime [15].

The time dependence of the population at the upper molecular level, n_2, can be described by the following differential equation [4, 8],

$$\frac{dn_2}{dt} = b_{12} I_\nu n_1 - A n_2 - Q n_2 - b_{21} I_\nu n_2 \,. \tag{2}$$

Here I_ν is the laser spectral irradiance and n_1 is the number density of molecules at the lower level. In the case of a short laser pulse of low laser intensity, the upper-state population, changes temporally after excitation in the following way, as described in [5],

$$n_2(t) = n_2(\tau_L) e^{-(A+Q)t} \,. \tag{3}$$

Here $n_2(\tau_L)$ denotes the number of molecules excited into the upper state by a laser pulse of length τ_L. The expression just shown includes a clear single-exponential decay term and can thus be related to the general form of a single-exponential function, i.e. $I=I_0 e^{-t/\tau}$. This means that the collisional quenching that occurs can be determined by measuring the fluorescence lifetime, τ [15], since

$$\frac{1}{\tau} = A + Q \,. \tag{4}$$

The spontaneous emission, A, can often be neglected, since it is typically 10^3 times weaker than the quenching effects and $\tau \approx Q^{-1}$ [15]. The average quenching rate of a system can be calculated by summing over the species-specific quenching cross section σ_i, the average thermal collision velocity $\langle v_i \rangle$, and the concentration n_i, of the quencher species i [4],

$$Q = \sum \sigma_i v_i n_i \,. \tag{5}$$

The average thermal collision velocity is given by

$$\langle v_i \rangle = \sqrt{\frac{8k_B T}{\pi \mu_i}} \tag{6}$$

where k_B is the Boltzmann constant, T the temperature, and μ_i the reduced mass of the quencher species i. The fraction of the excited molecules that emits fluorescence signals is referred to as the fluorescence quantum yield, Φ. This can be described as follows when collisional quenching is the dominant deactivation process,

$$\Phi = \frac{A}{A+Q} \approx \frac{A}{Q}. \tag{7}$$

2.1.3 Laser-induced fluorescence generated by short laser pulses

Equation 1 is the general expression for a laser-induced fluorescence signal. When molecular excitation is performed with use of a short laser pulse of low intensity, the population in the lower state is much larger than that in the upper state, i.e. $n_1 >> n_2$. This means that a steady-state assumption is not valid and that the growth term ($b_{12} I_\nu n_1$) in Equation 2 is much larger than the upper-state depopulation terms [8]. Given that the laser pulse intensity is low, the last term in Equation 2 can thus be neglected and the population in the upper state during the laser pulse is then given by direct integration of the first part of the equation, so that $n_2 = b_{12} I_\nu n_1 \tau_L$ [8]. If the number density of the lower level is related to the total molecular number density, N, through the Boltzmann factor, f_B, which is the case if thermal equilibrium prevails, the generated signal induced by a short laser pulse can be expressed as [8]

$$S_{LIF} = N f_B b_{12} I_\nu \Gamma \tau_L \Phi F_{fl} V \frac{\Omega}{4\pi} \varepsilon \eta \,, \tag{8}$$

where Γ is the lineshape function describing the overlap between the laser spectral profile and the absorption line, F_{fl} is the fraction of the fluorescence detected through the detector bandpass. The other parameters are described in the same manner as previously.

2.2 Photofragment laser-induced fluorescence

2.2.1 Introduction to photodissociation

Figure 2(a) shows how a photon is absorbed between two energy states, each of which holding potential energies with both vibrational and rotational states, where fluorescence being emitted from the upper state following laser excitation. Several molecules possess an upper electronic state potential that are repulsive along the intermolecular coordinate, R_{DC}. That state does not contain any vibrational or rotational energy levels, and is termed unbound or repulsive excited electronic states. When a molecule having an upper-unbound state absorbs a photon, it breaks apart into fragments, and the excess energy is converted into translation and internal energy (vibrational, rotational and electronic energy) in the fragments. This phenomenon is termed photodissociation, sometimes referred to also as photolysis or photofragmentation, Figure 2(b) presents a schematic diagram of the process.

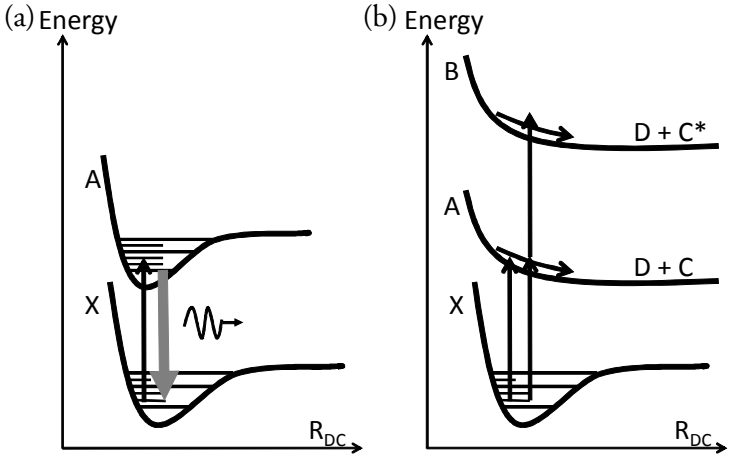

Figure 2 Schematic diagram of the UV excitation taking place (a) between two bound electronic states and (b) in a molecular system in which the upper state is unbound. The parent molecule (*DC*) consists of two atoms, *D* and *C*. When the upper state is unbound, the molecule dissociates into the fragments *D* + *C* after excitation. In (b) both single- and two-photon absorption is shown.

The photodissociation process can be described by the following expression,

$$DC + N_{photon} h\upsilon \xrightarrow{(1)} (DC)^* \xrightarrow{(2)} D(\alpha) + C(\beta), \tag{9}$$

where DC represents the parent molecule, $h\upsilon$ is the energy of a single photon with a frequency of υ and N_{photon} is the number photons that are absorbed. $(DC)^*$ denotes the excited parent molecule prior to its breaking apart into fragments D and C, where α and β designate the internal quantum state of the fragments. The process can be divided into two steps, the first step, (1), being the absorption of a photon by the parent molecule, this being followed by the second step, (2), which represents the fragmentation of the excited parent molecule.

The photodissociation of molecules can be carried out with photons from the gamma to the infrared energy regime, but is often performed using laser pulses in the UV regime. Traditionally, low-intensity light sources, such as conventional UV lamps or weak nanosecond laser pulses in the UV regime, have been used to investigate the dynamics of the photodissociation of molecules. During the last decade, extremely intense femtosecond laser pulses ($>10^{13}$ W/cm^2) have been used in spectroscopic studies of ionization and dissociation processes in molecules. The photodissociation processes are completely different for weak and strong laser photolysis, a weak light source resulting in single-photon excitation to low-lying repulsive electronic states, this implying that typically only one or two bonds in the parent molecule are broken. In contrast, photolysis using ultra-intense light sources results in multi-photon excitation to high-lying dissociative states, this causing the breakage of several bonds and the creation of a multitude of photofragments that also can be formed in an excited state. Multi-photon absorption can take place via either virtual or real states in the molecule. For excitation via a virtual state, photons of the same energy need to be absorbed simultaneously so that their energy coincides with one another in terms of both space and time. The process is thus favored by a high photon density being present during a short period of time, this being easily achieved by use of picosecond or femtosecond laser pulses. Two-photon dissociation via a real state is illustrated in Figure 2(b). Since the process takes place between real states, the two photons need not to be absorbed instantaneously in space and time.

2.2.2 Photofragmentation laser-induced fluorescence of hydrogen peroxides

As mentioned in the previous section, molecules in an unbound excited state cannot be detected by LIF. However, they can be measured indirectly by probing the fragments that have been created with LIF. This pump-probe technique is termed photofragmentation laser-induced fluorescence (PFLIF). Rogers et al. [16] were the first to propose use of this technique for the detection of trace species. Since then, the technique has become well established for the detection of several different species [17-22]. In the thesis work, PFLIF has been used for the detection of both hydrogen peroxide, H_2O_2, and the hydroperoxyl radical, HO_2, in different combustion systems. Both molecules have an unbound excited state, where UV excitation leads to dissociation into fragments, this resulting in a continuous featureless absorption spectrum [23]. The PFLIF scheme applied to H_2O_2 is shown in conceptual terms in

Figure 3. First, a UV laser pulse (a pump pulse) dissociates H_2O_2 into two OH fragments. After a short time delay, typically in the order of nanoseconds, a second laser pulse (a probe pulse), tuned to an absorption line in OH, excites the OH fragments and the induced fluorescence signal can be detected. The intensity of the fluorescence signal is proportional to the concentration of the OH fragments and thereby also to the concentration of hydrogen peroxide [24].

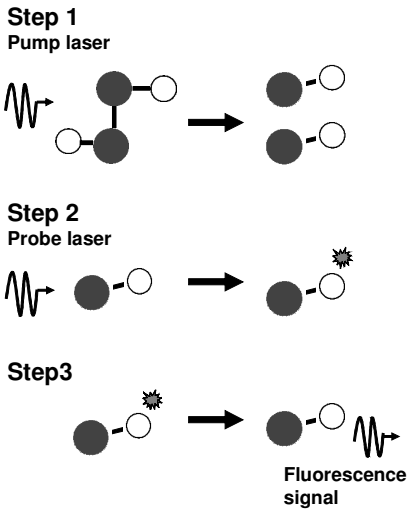

Figure 3 A schematic diagram of the pump-probe technique PFLIF as employed for H_2O_2 detection. A UV-laser pulse dissociates H_2O_2 into OH fragments (step 1) that later are probed by LIF (step 2), and the OH fluorescence is emitted (step 3), enabling the hydrogen peroxide to be measured indirectly.

Photofragmentation laser-induced fluorescence can be performed using either one or two lasers. In the work presented in the thesis, two different lasers were employed. The advantage of using two different lasers is the possibility it provides of optimizing the two processes involved, i.e. photodissociation and LIF detection. The pump wavelength can be selected so as to optimize the dissociation process through saturating the photodissociation, maximizing the concentration of fragments, as well as controlling the energy deposited in the fragments that are created. In addition, the wavelength of the probe beam can be selected to exploit a strong absorption line in the fragments, increasing the intensity of the fluorescence signal that is generated. The use of a two-laser setup enables pump-probe delay studies to be carried out in which the time delay between the two pulses is varied, this allowing dynamic processes in the molecules as well as chemical kinetics, to be studied. Using a time delay between the two pulses in the order of ten nanoseconds enables a potentially interfering signal induced directly by the pump pulse to be removed. The experimental setup is more complicated, however, mainly because of the overlap between the pump and probe pulse being a critical factor. When only one laser is employed, the probe laser that

excites the fragment, here OH, also acts as a pump laser source, to dissociate it from the parent species, here H_2O_2 and HO_2. The experimental setup makes it easier to align the optics, since the fragments are created and excited by the same laser pulse. A, single-laser setup, in contrast, obviously prevents a study were the pump-probe delay time is varied.

For weak single-photon photolysis, the number density of photofragments, N_{di}, that are produced can be estimated using the following equation [25],

$$N_{di} = N_i \phi_i \left(1 - e \left[- \frac{\lambda_{laser} \sigma_i(T) E_{laser}}{hcA_{laser}} \right] \right) \tag{10}$$

where N_i is the number density of the parent species, ϕ_i is the OH production in terms of quantum yield for the precursor i, λ_{laser} is the wavelength of the pump laser, $\sigma_i(T)$ is the temperature- and wavelength-dependent single-photon absorption cross-section, and A_{laser} and E_{laser} are the laser sheet area cross-section and the pulse energy, respectively. The other parameters have been described earlier. The OH production in terms of quantum yield was found to be 2 for H_2O_2 when dissociation was performed using wavelengths longer than 230 nm, so that two OH fragments are formed [26]. For HO_2, 2.75 eV of photon energy is required in order to create OH + O [27, 28], which then gives ϕ_i = 1. The number of OH fragments resulting from dissociation of the parent species i is strongly dependent upon the laser pulse energy and the probe volume. If the initial H_2O_2 or HO_2 concentration is known, the number density of the OH fragments that are created can be calculated using Equation 10. A theoretical value of the HO_2 number density in a methane/air flame was reported in Paper IV [29, 30], and was used to calculate the fraction of photodissociated HO_2 molecules as a function of the laser sheet area and the pulse energy; see Figure 4. The temperature-dependent absorption cross-sections of HO_2 were determined using the model reported in [31], together with temperature profiles from [30]. When N_{di}/N_i is 1, 100% of HO_2 is dissociated, and for small laser sheets, the amount of the OH fragments is easily saturated, even with use of low laser pulse energies. There are several advantages in saturating the dissociation process. For example, if the concentration of HO_2 or H_2O_2 is unknown, which typically is the case, it is possible to determine in qualitative terms the amount of the parent molecule that is present, determining it backwards from the OH-fragment LIF signal. To determine the concentration of parent species quantitatively, use of Equation 8 should also be considered.

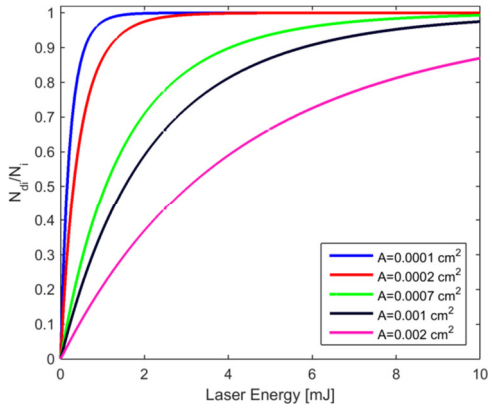

Figure 4 The calculated ratio of the amount of the photofragments produced, N_{di}, to the total amount of HO_2, N_i. The colors represents different laser sheet areas, A.

2.3 Picosecond vs nanosecond laser diagnostics in combustion

In laser-based combustion diagnostics, several different types of lasers can be used, the choice depending on the application involved. Traditionally, use is often made of Q-switched nanosecond lasers having a pulse duration of 5-20 ns and a 10 Hz repetition rate, due to their high peak power and robustness. The temporal resolution is ultimately defined by the pulse duration, which is in the range of 5-20 ns, a time scale on which flows and chemical reactions can mostly be considered as being frozen, allowing qualitative two-dimensional (2-D) imaging of species distributions in turbulent environments to be carried out. The repetition rate is not crucial in laminar flames and 10 Hz usually being adequate. To be able to follow turbulent flows and propagating flame fronts, lasers having at least kHz repetition rates are required [32, 33]. However, in applied combustion environments and in atmospheric-pressure flames, dynamic molecular processes such as collisional quenching, and rotational and vibration energy transfers occur on a very short time scale, the dephasing times of the excited states generally being in the order of 100 picoseconds up to nanoseconds. It is exceedingly important to understand how these processes affect the LIF signal, so as to be able to extract quantitative species concentration information, as already mentioned earlier in this chapter. These phenomena can be studied by use of laser pulses with a temporal width shorter than the fluorescence lifetime. This means that laser pulses having a duration in the order of 100 picoseconds or less are needed. The simulated LIF signals shown in Figure 5 demonstrate the difference between nanosecond and picosecond excitation. The nanosecond laser pulse has a width of 5 ns, whereas the picosecond laser pulse has a duration of 80 ps. As shown in the figure, it is barely possible to resolve the fluorescence decay at atmospheric pressure or above with use of a nanosecond laser.

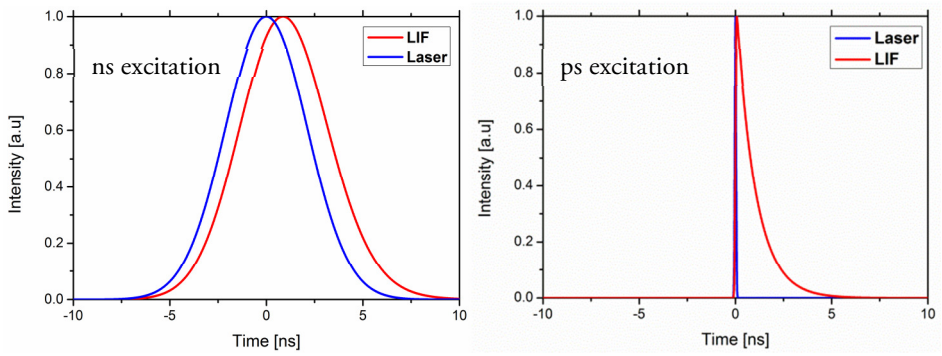

Figure 5 Illustrations of the differences, in the time domain, between nanosecond and picosecond excitation generating fluorescence signals at atmospheric pressure. The fluorescence signal is modeled as a single-exponential decay function having a 2-ns decay constant. The blue curves are Gaussian functions having a full-width at half maximum (FWHM) of 5 ns (left) and of 80 ps (right), these representing two very different laser profiles that later are convolved with the single-exponential function to generate the laser-induced fluorescence profiles that are shown (red curves).

Laser pulses that are shorter than the typical times for molecular dynamics are spectrally broader than the molecular absorption lines, the relation between the laser pulse duration and the bandwidth being dictated by the time-bandwidth product, which is $\Delta\tau\Delta\nu$=0.44 for a Fourier-limited Gaussian pulse [34], where $\Delta\tau$ is the pulse duration and $\Delta\nu$ is the laser bandwidth in Hertz. Thus, a short laser pulse results in spectrally broad radiation, and vice versa, thus there is a tradeoff between temporal and spectral resolution to take into account in using ultrashort laser pulses. To resolve rovibronic transitions spectrally, a narrow-linewidth laser, such as a nanosecond laser, is required, whereas finer structures, such as the hyperfine structure, require a single-mode laser in order to be resolved [35]. Picosecond laser systems in general have pulse energies in the millijoule (mJ) range. The peak powers are very high due to the pulse duration being very short, this facilitating the generation of nonlinear optical phenomena, such as two-photon excitation and sum-frequency generation.

3 Fluorescence lifetime studies

This chapter highlights and discusses briefly how fluorescence lifetimes can be measured in one- and two-dimensions in different combustion applications. Time-resolved fluorescence studies at a single point have been performed by several groups, these yielding quenching rates for a number of important combustion species, such as O [36], OH [37, 38], CO [39, 40], NO [41] and CH [42]. Thus far, there is only one previous study showing a method having the capacity to measure the quenching rate of a species single-shot, along a line [43]. Ehn et al. have developed recently a novel approach for two-dimensional fluorescence lifetime imaging [44]. The technique has been demonstrated for quenching correction of planar LIF images of formaldehyde recorded in a premixed CH_4/O_2 flame [45].

Paper I, in which the fluorescence lifetimes of CO and OH were measured simultaneously along a line in premixed flames will be discussed in Section 3.1. Paper II, in which Dual Imaging with Modeling Evaluation (DIME) for oxygen concentration imaging will briefly be discussed in Section 3.2.

3.1 One-dimensional resolved fluorescence lifetimes

3.1.1 Measurement approach

In the work presented in Paper I, one-dimensionally resolved dual-species measurements of OH and CO were carried out in a laminar methane/air flame on a Bunsen-type burner at four different equivalence ratios, ϕ = 0.9, 1.0, 1.15, 1.25. The equivalence ratio, ϕ, defines the ratio of fuel to oxidizer in a mixture to the stoichiometric fuel-oxidizer ratio. For a stoichiometric mixture in which ϕ = 1, there is a balance between the fuel and the oxidizer, and complete combustion occurs. A photograph of a flame at stoichiometric mixture is shown in Figure 6(a), the white line there representing the laser beam crossing the flame 9 mm above the burner. The work presented in Paper I constitutes the first demonstration of a measurement technique with the capacity to measure the fluorescence lifetimes of multiple species along a line in a single laser shot. The fundamental principle of the measurement approach here is to capture the fluorescence decay curves of two species simultaneously within a single streak on a streak camera. To capture OH and CO fluorescence under the present conditions, two tunable laser beams having a delay of ~3 ns between the two laser pulses was required. A temporal resolution of 100 ps,

covering a temporal range of ~10 ns, was used, which allows both the CO and OH fluorescence signals to fit within a single streak camera image. A typical image recorded 13 mm above the burner at ϕ = 1.25 is shown in Figure 6(b). The vertical axis is the radial distance within the flame, whereas the horizontal axis is temporal, providing a detailed analysis of the temporal and spatial characteristics of the two fluorescence signals. Figure 6(c) shows a temporal cross section corresponding to the area indicated by the dashed rectangle in Figure 6(b). By fitting a single-exponential function to the decay curves obtained in each pixel row in the streak camera image, spatially-resolved fluorescence lifetimes of CO and OH could be achieved.

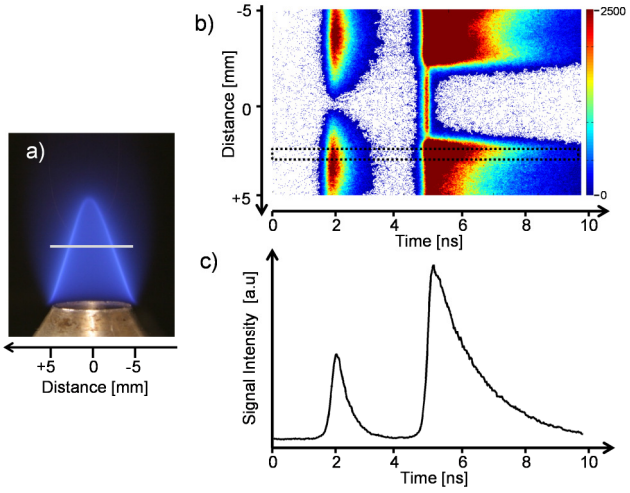

Figure 6(a) A photograph of the flame at ϕ = 1, the white line showing the laser beam crossing the flame 9 mm above the burner. (b) An accumulated streak camera image of CO and OH fluorescence recorded 13 mm above the burner at ϕ = 1.25. (c) An averaged signal indicated by the dashed rectangle in (b), the shorter CO fluorescence being followed by the longer OH fluorescence.

3.1.2 OH fluorescence lifetimes, quantum yields and quenching rates

By fitting a single-exponential function to the temporally resolved OH-fluorescence signal obtained in each pixel row of the streak camera image, radially-resolved fluorescence lifetime profiles could be obtained. OH lifetimes measured 9 mm above the burner for four different equivalence ratios are indicated by the symbols in Figure 7(a), whereas the corresponding calculated lifetimes are displayed by the solid lines there. Equations 4-6 were used to calculate the fluorescence lifetimes, while the quencher concentrations and the temperatures being predicted using the software CHEMKIN, making use of the GRI 3.0 chemical mechanism [46-50]. The quenching cross sections were calculated using the expression developed by Heard

and Hendersson [51] together with temperature profiles calculated on the basis of the GRI 3.0 mechanism. The OH fluorescence quantum yield is shown in Figure 7(b), the symbols again indicating the measured quantum yields, the lines corresponding to the calculated values. The Einstein coefficient for spontaneous emission used in the calculation is $1.451 \cdot 10^6\ s^{-1}$ [52]. From the results shown in panel (b) it can be concluded that approximately 99.7% of the excited OH radicals present in the product zone lose their excess energy through collisional quenching, rather than through the emission of fluorescence. The discrepancies between the measured results and the calculated data were found to stem from the adiabatic assumption regarding the flame and the uncertainty of the cross section for quenching with H_2O. Obviously, assuming adiabatic temperatures overpredicts the temperatures in the flame, which in turn leads to overpredicting the fluorescence lifetimes, since the lifetime is proportional to $\sqrt{T}$ (from Equations 4 - 6).

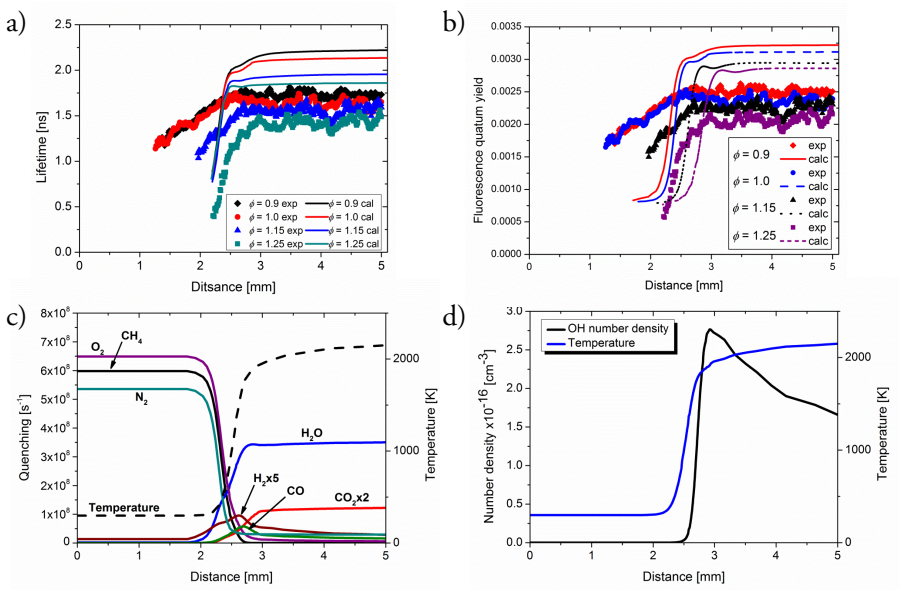

Figure 7(a) One-dimensional experimental (symbols) and calculated (solid lines) OH fluorescence lifetimes obtained in a methane/air flame at different stoichiometrics. (b) The corresponding OH fluorescence quantum yields. (c) The calculated radial quenching dependence of the species that collide with OH at ϕ = 1.0. (d) OH number density (black line) and adiabatic temperature profile (blue line) at ϕ = 1.0 from the GRI mechanism.

The calculated total quenching of OH is assumed to be very much dominated by collisions with the major species in the flame, i.e. N_2, O_2, H_2, CH_4, H_2O, CO_2, and CO. Their individual quenching rates, Q_i, at ϕ = 1.0 are plotted in Figure 7(c), together with the adiabatic temperature. It can be seen that H_2O is responsible for more than 80% of the quenching in the product zone. It is thus particularly important to use an accurate value for the quenching cross section of H_2O. The H_2O

cross section of 25.5 Å^2, derived by Heard and Henderson [51], appears to be somewhat low as compared with H_2O cross sections measured at flame temperatures (1300–1600 K) reported in the literature, i.e. 29 Å^2 [53], 29 Å^2 [54], and 26 Å^2 [55]. The somewhat low quenching cross section used for H_2O generates a 10% over-prediction of the lifetimes in the product zone. Rayleigh scattering experiments in the product zone of the stoichiometric flame resulted in a temperature of 1800 ± 50 K. Using this temperature in the calculations results in a shortening of 17% of the lifetimes found in the product zone. Thus when accounting for the under-estimated quenching cross section for H_2O and the over-estimated temperature, the result is a lifetime of 1.60 ns in the product zone, which is in excellent agreement with the corresponding measured lifetime, i.e. 1.63 ns ± 0.05 ns. Also, the OH fluorescence lifetimes measured in the product zone agree rather well with previously reported point measurements obtained in CH_4/air flames [15, 37, 38, 56, 57]. Figure 7(d) shows the calculated OH number density and the adiabatic temperature at ϕ = 1.0. It can be seen here that OH is formed in the reaction zone as the temperature increases and that the concentration attains a relatively high value (~0.5% mole fraction at a 5-mm distance) in the product zone of the flame.

Figure 8 shows the OH fluorescence signal collected 9 mm above the burner at ϕ = 1.0, together with the corresponding signal after division by the fluorescence quantum yield that is shown in Figure 7(b). As can be seen, variations in the fluorescence quantum yield have a rather strong effect on the spatial profile of the OH fluorescence signal. In the reaction zone, the correction leads to a signal increase, whereas in the product zone it leads to signal decrease. In addition, the correction results in a peak of the OH signal being located in the reaction zone, which is not present in the uncorrected profile, and a similar structure is also present in the calculated OH concentration profile, as shown in Figure 7(d). It is notable that the OH signal in the preheat zone is non-zero, this being due to the interfering Rayleigh scattering signal, as can be seen at the center of Figure 6(b).

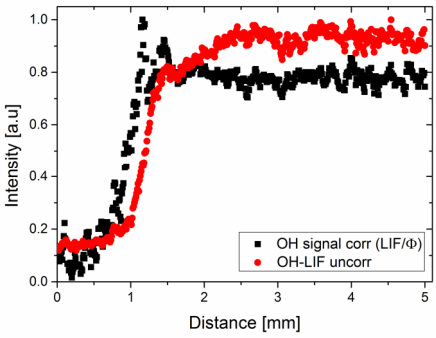

Figure 8 Spatial profile curves of the raw OH fluorescence signal (red dots) and the quantum-yield-corrected fluorescence signal (black squares) at a height of 9 mm above the burner at ϕ = 1.0. The curves are normalized to their peak values.

As already pointed out, correcting for fluorescence quantum yield is a necessary procedure for the extraction of quantitative concentrations from LIF data. To obtain absolute species concentrations, all the parameters in Equation 8 would need to be determined. The parameters that are the most difficult to determine, except for the fluorescence quantum yield, are those that are dependent upon the combustion environment, i.e. the Boltzmann factor, f_B, and the lineshape function, Γ. Both of these quantities are temperature-dependent, and Γ is also pressure-dependent. Thus, knowledge of both the temperature and the pressure is required. In the present work, a picosecond laser pulse of 308.95 nm was used for OH-LIF. Due to the relatively broad spectral width of the picosecond pulse (0.05 nm), several absorption lines are covered by the laser, primarily $Q_1(7)$ but also $Q_2(2)$ and $Q_2(3)$, which complicates the treatment of the Boltzmann factor and the lineshape function. The temperature-dependent fractional populations for N = 2, 3, and 7, respectively, are shown in Figure 9. From Figure 7(d) it can be seen that the OH concentration is only significant for temperatures above ~1000 K. For this reason, only temperatures above 1000 K need to be considered in Figure 9. It can be seen in this regime that the population at N = 7 is fairly constant, whereas the populations at N = 2 and 3 decrease with increasing temperature. Thus, neither the Boltzmann factor nor the lineshape function was accounted for in the present work. For quantitative measurements it is thus preferable to select an isolated absorption line, or to select transitions for which the population and the lineshape function have a weak temperature dependence.

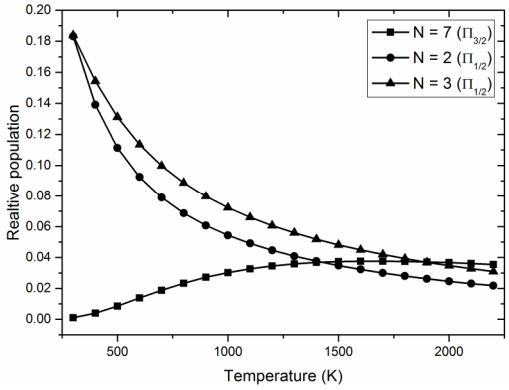

Figure 9 A plot of fractional populations for N = 3 (triangles), N = 2 (dots) and N = 7 (squares) in the electronic ground state of OH shown as a function of the temperature.

3.1.3 CO fluorescence lifetimes, quantum yields and quenching rates

For CO, due to the weak fluorescence signal, the streak camera pixels were binned in groups of 10 pixels rows each in the vertical direction, before a single-exponential

function was fitted to determine the fluorescence lifetime. For the calculated lifetime, CO is assumed to collide with the same species as OH. Quenching cross sections for species colliding with CO were calculated using the temperature-dependent expression derived by Settersten et al. [58] together with temperature profiles from the CHEMKIN simulations. Measured lifetimes are presented as symbols in Figure 10(a), whereas calculated lifetimes are shown as lines. The fluorescence measured in the two leanest flames (ϕ = 0.9 and 1.0) had low signal-to-noise ratios, this resulting in considerable scattering of the data points, and they are therefore not presented in the plot. The CO fluorescence lifetime does not depend on the flame stoichiometry in the same way as the OH fluorescence does. In the product zone, the mean value of the fluorescence lifetimes measured for the four different equivalent ratios was found to be 0.34 ns. The corresponding value for the calculated lifetimes is 0.35 ns, which is thus in excellent agreement with the experimental result. By choosing non-sooty flames, problems due to C_2 interferences are minimized [59, 60]. Issues due to predissociation and ionization were reduced, since excitation was carried out for rotational levels of less than J' = 37, for which predissociation is expected to be insignificant, the laser fluence also being kept sufficiently low to reduce ionization effects [61, 62].

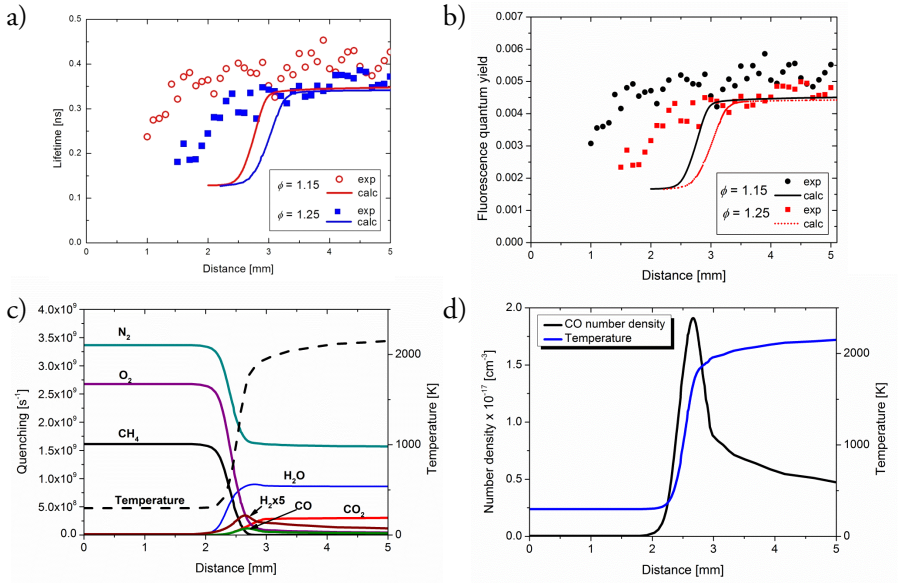

Figure 10(a) One-dimensional experimental (symbols) and calculated (solid lines) CO fluorescence lifetimes in a methane/air flame at ϕ = 1.15 (red circles and line) and 1.25 (blue squares and line). (b) Corresponding CO fluorescence quantum yields. (c) The calculated radial quenching dependence of the species colliding with CO at ϕ = 1.0. (d) The CO number density (black line) as predicted by the GRI 3.0 mechanism together with the adiabatic temperature profile (blue line) at ϕ = 1.0.

Since the CO fluorescence lifetimes were only ~4 times as long as the laser pulse duration, it is important to consider only the latter part of the fluorescence decay curve in the data analysis. In Figure 10(b), the CO fluorescence quantum yield is presented. Here, the rate of spontaneous emission is assumed to be $1.3 \cdot 10^7$ s^{-1} [40]. Although CO has a much shorter lifetime than OH, there were again around 99.6% of the excited molecules that were found to lose their excess energy via radiationless deexcitaion rather than through the emission of fluorescence.

In Figure 10(c), the individual quenching rates, Q_i, for each species i colliding with CO are presented, together with the adiabatic temperature profile. As can be seen, N_2 and H_2O are the two dominant quencher species in terms of the shape of the CO lifetime curves. Nitrogen has a significant quenching rate in the preheat zone as well as in the product zone, where the quenching by H_2O also is substantial. The calculated CO number density and an adiabatic temperature profile are presented in Figure 10(d). As can be seen, CO is formed and present in the reaction zone, whereas the concentration decreases in an outward direction so as to attain a relatively constant value in the product zone.

3.2 Two-dimensional fluorescence lifetime imaging

In the work presented in Paper II, fluorescence lifetimes of toluene as a function of the oxygen concentration in toluene/nitrogen/oxygen mixtures were measured at room temperature. The newly developed fluorescence lifetime imaging scheme DIME was used for quantitative oxygen concentration imaging. Details concerning DIME are to be found in works by Ehn et al. [44, 45, 63]. The basic principle behind the technique is that quantitative experimental results are achieved by a comparison between simulated intensity ratios and experimental intensity ratios. For this to be done effectively, the experimental setup needs to be characterized in great detail.

By first determining the relationship between the toluene fluorescence lifetimes in different oxygen mixtures, quantitative oxygen concentrations were obtained by utilizing the Stern-Volmer relationship. An image of the oxygen concentration could then be obtained from the fluorescence lifetime data that were generated by DIME. In DIME, two images are recorded with use of different camera gates, short, I_{sg}, and long, I_{lg}, for measuring different parts of the signal decay involved, in our case the toluene fluorescence decay signal. By overlapping the two images pixel by pixel, a ratio image was formed, $R_e = I_{sg}/(I_{sg} + I_{lg})$, where the variations in intensity are due to local differences in the fluorescence decay that occur. Accordingly, inhomogeneities in the laser profile and variations in concentrations were cancelled out. To obtain quantitative fluorescence lifetimes from the ratio image, the fluorescence signals detected by the two camera gates were simulated. Since the fluorescence signal S is assumed to possess single-exponential decay, it was possible through knowledge of the laser pulse temporal profile, the timer jitter and the camera-gain function, G_i, to

calculate the fluorescence signal I_i as detected by the ICCD camera, for different fluorescence lifetimes, τ,

$$I_i(\tau, t_i, \delta) = \int_{-\infty}^{\infty} S(t, \tau) G_i(t - t_i - \delta). \tag{11}$$

The variables t_i and δ are the camera delay time and the time-jitter, respectively. Since creating a library of simulated ratios R_s for a range of different fluorescence lifetimes meant that a specific value of R_s would correspond to exactly one fluorescence lifetime, each pixel in the experimental ratio image could be converted into an image representing the toluene fluorescence lifetime, which then corresponded to a specific concentration of oxygen.

4 Laser-induced fragmentation

This chapter reviews the photodissociation process that occurs when a laser pulse of 266 nm excites different types of stoichiometric hydrocarbon/air flames on the coaxial burner used in the work presented in Papers III-VI. Being the fourth harmonic of the Nd:YAG laser, the 266-nm pulse can be generated in a straightforward way, possessing a fairly smooth Gaussian profile and having the possibility of a high pulse energy being maintained. Section 4.1 reports on the observed emissions from the reaction zone of hydrocarbon/air flames, induced by a nanosecond 266-nm pulse having a fluence of ~$2 \cdot 10^8$ W/cm^2. Section 4.2 reviews the observed fluorescence from the unburnt zone of a methane/air flame induced by a picosecond laser pulse at laser-pulse intensities of ~$2 \cdot 10^{11}$ W/cm^2 (Paper III). The two cases differ completely in the photodissociation process involved. With the nanosecond laser pulse, few of the bonds in the molecules present in the reaction zone of the flame are broken, and the luminescent fragments are created through chemical reactions. In contrast, the picosecond laser pulse is absorbed through multi-photon excitation leading to multiple breakages of several bonds of the methane molecule in the unburnt zone, this resulting in the creation of several luminescent fragments.

4.1 Nanosecond fragmentation in hydrocarbon/air flames

A strong fluorescence emission from the reaction zone was observed when a 5-nanosecond laser pulse of 266-nm excited stoichiometric mixtures of air and different hydrocarbon fuels. The emission was collected with a gated ICCD camera equipped with a UV-objective and spectrally filtered by a combination of a UG11 and a WG305 filter. The camera had a gate width of 50 ns that strongly suppressed the chemiluminescence of the flame. A cross-sectional profile of the signal that was generated was achieved by vertical integration of the signal obtained in the accumulated images. Figure 11 shows emission profiles obtained in methane, ethane and propane flames, as well as an OH-LIF signal acquired after 282.16-nm excitation in the propane/air flame. Comparing the signal induced by the 266-nm pulse with the OH fluorescence, it was concluded that the strong signal that is induced is isolated in the reaction zone, and that the strength of the signal provides the possibility of single-shot imaging of the reaction zone in turbulent flames. There was a strong correlation between the strength of the induced signal and the amount of carbon in the fuel. To further investigate the origin of the emission from the flame,

the signal was collected and resolved using a spectrograph coupled to a gated ICCD camera.

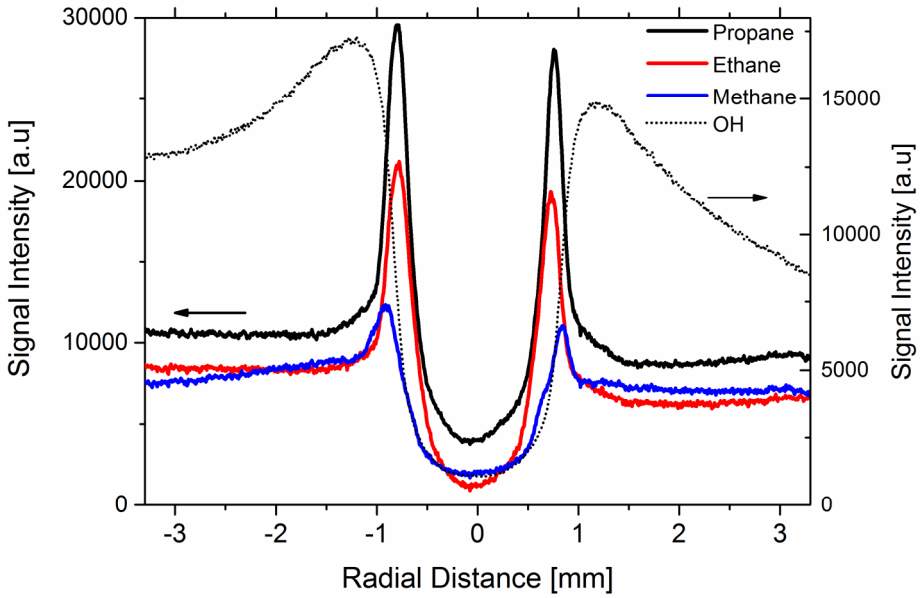

Figure 11 Radial profiles obtained in three different flames consisting of a stoichiometric mixture of air and either propane (black), ethane (red) or methane (blue). The dotted black line corresponds to the OH fluorescence obtained in the propane/air flame through the OH radical being excited by a 282.16-nm laser pulse. The strength of the OH-LIF signal is shown on the right axis of the graph.

Figure 12 presents an image of the spectrally resolved emission that was induced in the propane/air flame by the 266-nm laser pulse, where the radial distance in the flame is shown on the y-axis and the wavelength on the x-axis. The flame is symmetric and the three zones are indicated for one side of the flame. Note that the emission corresponds to fluorescence from electronically excited species and from Raman scattering. The signal in the product zone stems from OH(A-X) fluorescence emission in the (0,0) and (1,0) bands, since the wing of the 266-nm spectral laser profile can excite the $Q_2(13)$ absorption line in the (2,0) vibronic OH band. The signal from the unburnt zone stems from Raman scattering of propane, oxygen and nitrogen, and also to a minor extent from OH emission in the reaction zone that stream into the unburnt zone. The signal from the reaction zone is caused by emission from several different species. To investigate the emission from the reaction zone further, the integrated signal denoted in Figure 12 by the box is presented in Figure 13 as a spectrum.

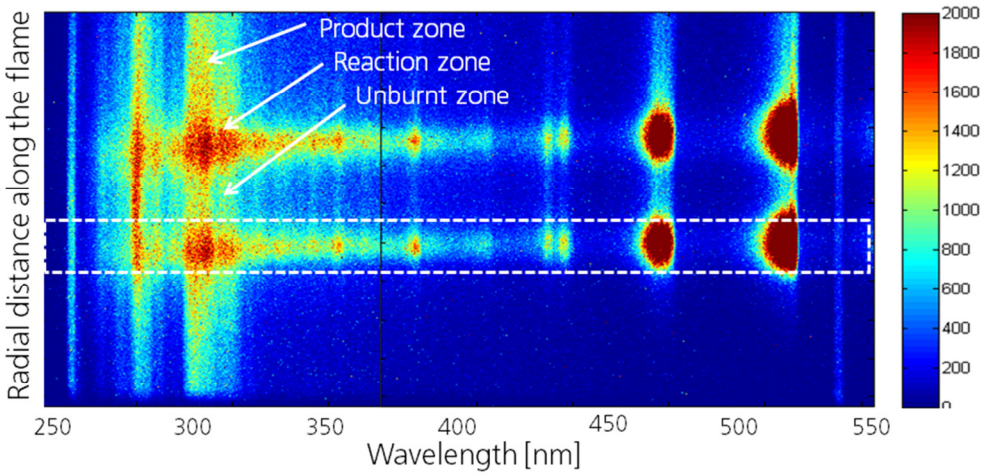

Figure 12 A low-resolution spectrally-resolved emission image obtained in a propane/air flame. The spectrometer has a grating with 150 grooves/mm and a slit width of 200 µm, the camera gate being open for 100 ns.

The spectrum obtained from the reaction zone, shown in Figure 13(a), is similar to a chemiluminescence spectrum from a propane and air flame of stoichiometric mixture. Raman scattering from O_2, N_2 and C_3H_8 is observed at 277, 284 and 288 nm, respectively, while the emission between 305 and 320 nm is OH(A-X) fluorescence mainly in the (0,0) and (1,1) bands. The two marked peaks at 474 and 517 nm correspond to C_2 emissions in the Swan bands. The spectral features at 420-440 nm can be assigned to the fluorescence from CH(A-X) that is superimposed upon the C_2 peak at 436 nm. In the region of 305-420 nm, fluorescence from several species is visible and Figure 13(b) shows part of the spectrum zoomed in. The peaks at 358, 388 and 418 nm correspond to different vibrational bands, Δv=-1, 0 and +1, respectively, of the B-X transition in CN. In addition, the spectral features at 305-320 and at around 345 nm can be assigned to the CH(C-X) transition, along with the OH(A-X) transition in the (0,0) and (1,1) bands. The peak at 336 nm corresponds to the NH(A-X) transition. Finally, the spectral features at around 365, 387 and 405 nm can be assigned to the CH(B-X) band. There, nevertheless, are still some peaks that have not been identified. It is known that HCO has several emission lines in the 280-420 nm region [64, 65]. Thus, the peaks at 330 and 350 could for example be due to emissions from HCO. The signal peaks between approximately 275 and 420 nm sit on the top of a broadband signal contribution that most likely represents fluorescence from polycyclic aromatic hydrocarbons (PAH) that are formed as intermediates in hydrocarbon flames and that absorb light in the UV regime. Their fluorescence signal appears in the range of approximately 250-350 nm [66].

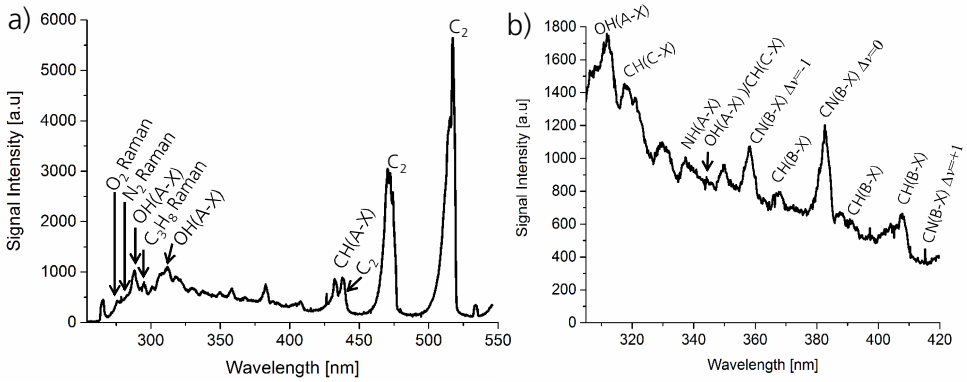

Figure 13(a) A low-resolution spectrum of the emissions from the reaction zone of a propane/air flame induced by a 5-nanosecond laser pulse at 266 nm. (b) A spectrum in the region of 305-420 nm.

The fragments observed are in electronically excited states since their fluorescence emission can be detected. By moving the camera gate in steps over the induced emission it was found that fluorescence still can be detected even when the gate is delayed by 10 ns from the 266-nm pulse. A 266-nm photon corresponds to 4.66 eV and this energy is more than enough to photodissociate single bonds in larger hydrocarbons that are present in the reaction zone of the flame. The excess energy is probably not sufficient, however, for excitation of the fragments that are created. Thus, the fragments are most likely created in excited states via chemical reactions.

Previous work demonstrates the possibility of using a 266 nm tunable Nd:YAG-laser to simultaneously image the product and the unburnt zone of a hydrocarbon flame through exciting OH in the product zone via the (2,0) rovibronic band and simultaneously exciting acetone that is seeded into the unburnt zone [66]. The present study demonstrates the 266-nm beam being potentially able to visualize all three zones in a flame simultaneously. It also points to the importance of having an adequate delay time between the pump and the probe pulse in PFLIF experiments so as to avoid interfering signals from the reaction zone that could potentially overlap with the LIF signal from the photofragments.

4.2 Picosecond fragmentation in room-temperature CH_4/air gas

During the past decade, extremely intense femtosecond laser pulses (>10^{13} W/cm^2) have been used in spectroscopic studies of ionization and dissociation processes in several hydrocarbons, methane in particular [67-73]. In Paper III, the emission spectra from the methane dissociation induced by a focused 266-nm picosecond pulse of intermediate intensity, one of $2.0 \cdot 10^{11}$ W/cm^2, is discussed. Figure 14 shows a

spectrally resolved image of the signal induced in a methane/air flame by an 80-picosecond laser pulse. In comparing this image with Figure 12, it can be seen that the induced signal shown in Figure 14 stems mainly from the unburnt zone of the flame, as indicated by the dashed box. The signal contribution in the product zone is most likely from OH that has been excited in the (2,0) band. The minor fluorescence signal found in the reaction zone is from signal contributions from the unburnt zone.

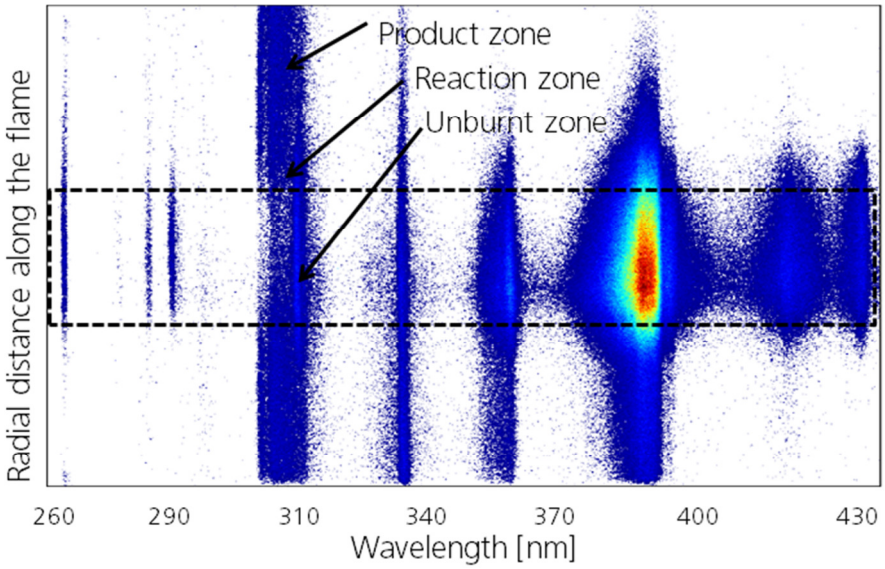

Figure 14 A low-resolution spectrally-resolved induced-emission image obtained by an 80-picosecond pulse at 266-nm wavelength in a methane/air flame at stoichiometric mixture.

To further investigate the photodissociation process, spectrally resolved images were recorded in methane/air mixtures at room temperature. The black spectrum in Figure 15 shows a low-resolution fluorescence spectrum, whereas the red spectra represent emission features recorded at high spectral resolution. The fragments identified, CH(A-X, B-X, C-X), CN(B-X, Δv = 0 and Δv = ±1), NH(A-X), OH(A-X) and N_2^+(B-X), are denoted in the figure, together with the three Raman lines corresponding to O_2, N_2 and CH_4, respectively. The spectrum does not contain any spectral features from atoms, such as those of H, O, C, or N, and the background level is rather low. It is of interest to note that no spectral features from the C_2 Swan bands were observed when analyzing the spectral region 430-650 nm. In addition, there was no spark, i.e. no white-light emission indicative of breakdown or plasma formation, visible in the laser beam focus. These observations indicate little or no plasma formation in the measurement volume, despite highly excited molecular fragments being created.

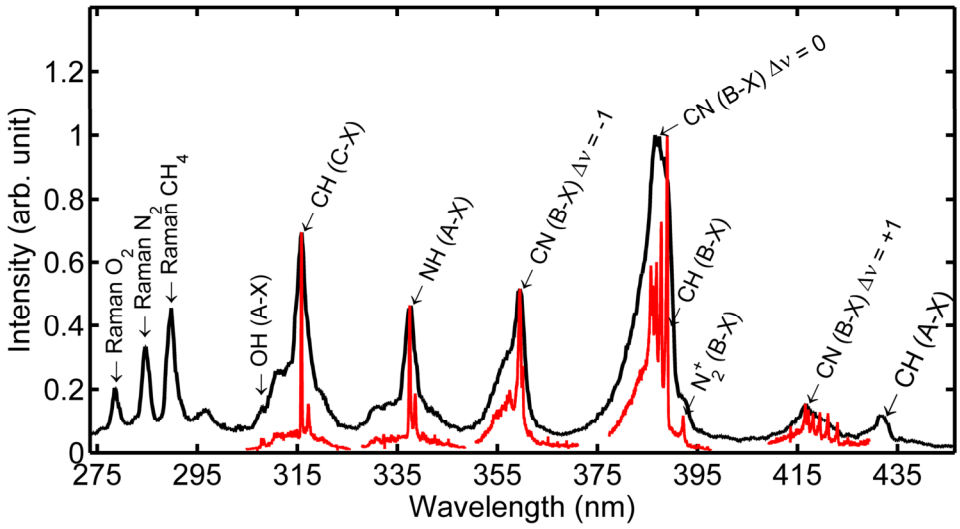

Figure 15 A low-resolution emission spectrum (black) induced by intense 80-picosecond laser pulses in the free flow of a stoichiometric mixture of CH_4/air. The fragments and the associated transitions that were identified are denoted in the figure. The red spectra were recorded by the high-resolution grating (1200 groves/mm) in the spectrograph.

The fact that fragments are created in electronically excited states means that excess energy is available in the fragmentation process. There is at least an excess of energy great enough to electronically excite the fragments observed via their fluorescence. To examine these properties further, the highly-resolved experimental spectra were compared with simulated spectra. Fluorescence spectra corresponding to CH(C-X), OH(A-X), and CN(B-X) were simulated using LIFBASE [52], whereas NH(A-X) fluorescence was simulated with PGOPHER [74], molecular constants from [75] being employed. The simulated spectra were fitted to the measured spectra, using rotational and vibrational temperatures as fitting parameters, and the Boltzmann distributions of the rotational and vibrational populations was retained. It was found that all neutral fragments that were observed were created in a state of highly non-thermal equilibrium, corresponding to rotational and vibrational temperatures ranging from 2000 to 8000 K. This suggests that the chemical reactions involved in producing OH and NH, and in particular CN, are highly exothermic.

To investigate the dissociation process in methane further, the dependencies of the fluorescence signal on the laser-intensity and on the CH_4/air equivalence ratio were studied for each fragment. On the basis of the signals obtained, CH was found to be linearly dependent upon the laser pulse energy. It was hypothesized that CH(A,B,C) is formed through neutral dissociation via a super-excited state of CH_4, reached by 3-photon excitation, and that 2-photon ionization/dissociation rather than collisional quenching is dominant in the deactivation of the CH fragments. Thus, one possible explanation for the observed intensity dependence of the CH fluorescence could be

the combination of a 3-photon production term and a 2-photon consumption channel. In addition, NH(A) and CN(B) were found to be created by 3-photon excitation of CH_4, whereupon hydrogen and carbon then reacting with nitrogen to create NH and CN. The dependence of the signal on the equivalence ratio suggests that NH formation is linked to the present nitrogen concentration, whereas the formation of CN is more strongly coupled with the methane concentration. Not surprisingly, the CH formation was found to be directly linked to the methane concentration.

To further investigate the formation and consumption of the photofragments, spectrally and time-resolved measurements were carried out by coupling a streak camera to a spectrograph. Figure 16 shows a streak-camera image obtained in this way, both the photofragments and the Raman scattering from CH_4 are denoted.

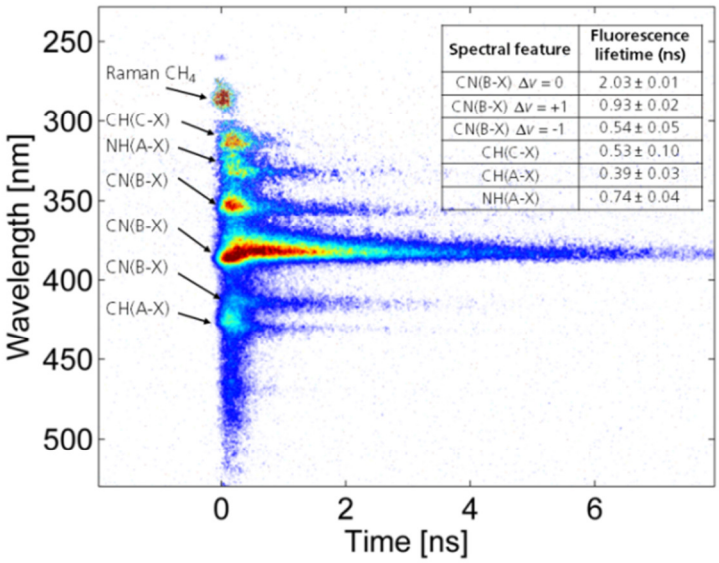

Figure 16 A spectrally resolved streak-camera image of the emission induced by the picosecond laser in a stoichiometric CH_4/air gas mixture. The fragments that were identified are denoted. *Inset*: A table showing the fluorescence lifetimes as determined from the early part of the fluorescence signals.

From the figure it was found that all observed fragments are formed within 200 ps after the arrival of the laser pulse. By binning the pixels in the vertical direction across the entire signal for each fragment, the integrated fluorescence lifetimes, corresponding to all the rovibronic transitions that occurred within each fluorescence band, were determined. The measured fluorescence lifetimes are listed in the inset of Figure 16. It is notable that all of the fluorescence decays are bi-exponential. The early part of the fluorescence signals have lifetimes shorter than 1 ns, except for the CN(B-X) $\Delta v = 0$ fluorescence, which has a single-exponential decay with a lifetime of

2.0 ns. The latter part of the signals, were found to be 2.3 ± 0.5 ns for all of the fluorescence curves that were investigated. Even if the lifetimes appear to be somewhat short, the measured NH(A-X) fluorescence lifetime is relatively close to the calculated lifetime, and the CN(B-X) $\Delta v = 0$ fluorescence lifetime is close to CN lifetimes as measured previously in a $CH_4/N_2O/N_2$ flame [76]. In addition, the lifetime of the CH(A-X) fluorescence is calculated here to be 8 ns, which is in agreement with the CH lifetime measured by Xu et al. [69]. This lifetime is about 20 times as long as the measured lifetime here (0.39 and 0.53 ns). As was suggested earlier, CH(A,B,C) might perhaps be depopulated by 2-photon photoionization, a matter that could explain the short lifetimes of CH that were found.

The results presented in this section again emphasize the importance of having an appropriate delay time between the pump and the probe pulses in PFLIF experiments in flames. A proper time delay is necessary to avoid interfering signals from photofragments being created as a result of methane dissociation in the unburnt zone. The fluorescence lifetimes of the induced fragments were found to be around 2 ns. Thus, by having a steep gate function on the camera synchronized with the probe laser, it should be possible to perform PFLIF experiments with use of picosecond laser pulses having a pump-probe delay time of at least 2 ns. In Paper III, the possibility is discussed of using the multitude of luminescent fragments obtained as the basis for a method of measuring the local fuel equivalence ratio in methane/air mixtures [77].

5 PFLIF for combustion imaging

This chapter reviews the work presented in Papers IV-VI, in which PFLIF is used to measure hydrogen peroxides in the reaction zone of laminar methane/air flames. In the work presented in Paper IV, hydrogen peroxides are visualized for the first time in two-dimensions in laminar hydrocarbon flames through the use of nanosecond-PFLIF. The paper also discusses the chemically produced interfering signals observed in the product zone. In the work presented in Paper V, in turn, PFLIF is carried out for the first time with use of picosecond laser pulses for studying the initial rotational population in the OH fragments that are created in the reaction zone of the flame. In addition, the temporal development of the OH-fragment signal in the reaction zone is analyzed. Paper VI, presents a method enabling single-shot imaging of hydrogen peroxides in flames to be carried out.

5.1 Introduction to PFLIF in flames

Hydrogen peroxide, H_2O_2, and the hydroperoxyl radical HO_2, are important intermediate species in various oxidation processes, such as in plasma, combustion and atmospheric chemistry. In the troposphere, OH is the most important oxidant and it is produced primarily by the photolysis of O_3, where its chemistry is closely linked with the chemistry of HO_2 and H_2O_2 [78, 79]. In hydrocarbon combustion, the molecules are important flame intermediates, where they are playing a key role in the low-temperature (<1200 K) oxidation of fuel [80], as well as in high-temperature H_2/O_2 combustion systems in which the initiation reaction $H_2 + O_2 \rightarrow HO_2 + H$ is essential [81]. It is also well known that the thermal decomposition of hydrogen peroxides is an essential chain-branching reaction that is dominant in hydrocarbon autoignition in various combustion engines [82-84], a matter that will be discussed further in Chapter 6. In practical industrial applications, H_2O_2 is used, for example, for sterilization of food packaging material [85].

Hydrogen peroxides have been detected previously in combustion environments using various absorption-based techniques [86]. These methods are attractive for measuring absolute species concentrations, since the signal involved is unaffected by quenching and predissociation. The measured absorption signal, however, is integrated along the line of sight, and measurements are thus restricted to volumes in which variations in concentration and temperature along the line of sight are insignificant. It is thus evident that there is a strong need for a technique that enables

HO_2 and H_2O_2 to be detected in-situ with a high degree of species selectivity and a high level of spatial and temporal resolution.

The three papers of relevance, Papers IV-VI, deal with two-dimensional imaging of hydrogen peroxides in premixed laminar flames by using a 266-nm pump pulse and a probe pulse exciting the OH fragments in the (1,0) band. There are various challenges to account for in employing PFLIF for flame diagnostics, one major challenge being the potential interference from other species that produce OH fragments. It has been found, based on knowledge of species concentrations obtained from CHEMKIN-II, making use of the Konnov detailed C/H/N/O reaction mechanism [29], that, in addition to HO_2 and H_2O_2, 23 other species could in principle be OH photofragment precursors in a stoichiometric methane/air flame. All of them, except for CH_3O_2, could be rejected as direct parents of OH fragments, however, for any (one or more) of the following reasons: too low concentration, too low absorption cross section at 266 nm, too low OH production quantum yield, and/or predicted spatial location. Thus, OH fragments from CH_3O_2 would interfere with OH fragments created by the dissociation of HO_2 and H_2O_2 [87, 88]. The contribution of OH fragments from CH_3O_2 was found, however, to be very small, making up less than 1% of the total signal in the reaction zone in a stoichiometric methane/air flame.

Furthermore, a major challenge in applying PFLIF for flame diagnostics is the strong interfering signal from the naturally present OH radicals, which are excited by the probe beam in the same way as the OH fragments. HO_2 and H_2O_2 are present in the reaction zone, whereas natural OH is located predominantly in the product zone, with a sharp concentration gradient in the reaction zone, see Figure 7(d). Hence, the signal contribution from OH fragments tends to spatially overlap with the signal from the naturally present OH. To deal with this matter, two images were recorded. First, a LIF measurement was performed with firing of only the probe pulse, this resulting in an image that only contains signal from the OH which is naturally present. After that, both the pump and probe pulses were fired (PFLIF), this resulting in an image that contains fluorescence signal from both naturally present OH and OH fragments. By subtracting the first image (LIF image) from the second image (PFLIF image), the resulting image would then only contain signal from OH fragments, which is related to the concentration of hydrogen peroxides [24]. This strategy was employed in the experiments reported in Papers IV and V.

Figure 17(a) presents a two-dimensional nanosecond-PFLIF image obtained in a CH_4/air flame on a coaxial burner. The major part of the signal stems from naturally present OH radicals. Figure 17(b) shows the signal that remains after subtraction of the LIF image. A razor blade was used to block the upper part of the photolysis beam to create a region in which the signal would be zero after subtraction of the LIF image. This procedure was undertaken in Paper IV, to make sure that no artificial signal contributions due to inaccurate subtraction would be present in the final image. On the basis of calculations, it was found that approximately 87% of the

integrated reaction zone signal at ±1 mm was due to OH fragments stemming from HO_2, whereas about 12% are from H_2O_2, the rest (~1%) coming from CH_3O_2 [30]. In the next section, the signal in the reaction zone will be discussed further. The signal present in the product zone, see Figure 17(b), does not stem from HO_2, it was instead found that this signal originates from the photolysis of hot CO_2, a matter that will be discussed further in section 5.3.

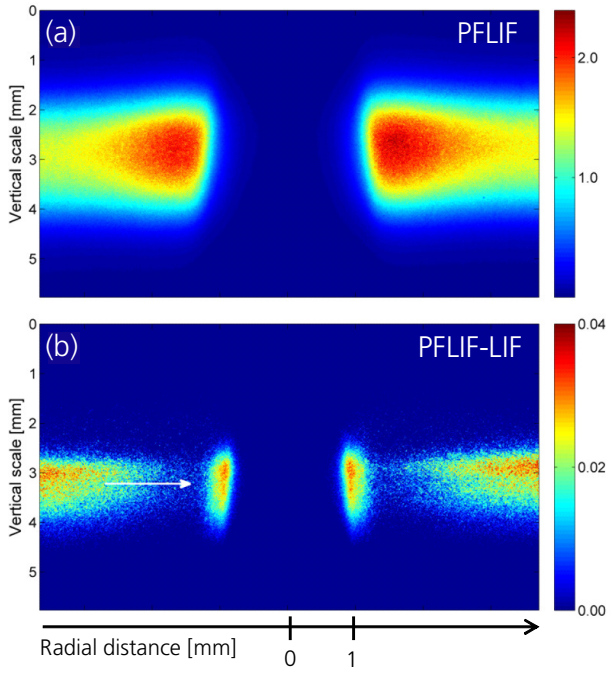

Figure 17(a) Typical 2-D PFLIF images recorded in a laminar methane/air flame at an equivalence ratio of 1.15. Both the pump and the probe lasers were fired. (b) An OH fragment image obtained from the PFLIF image after subtraction of the signal from the naturally present OH. The arrow points toward the reaction zone of the flame at the left.

To verify that the measured signal in the reaction zone indeed originated from OH, excitation spectra were recorded with use of nanosecond (Figure 6 Paper IV) and picosecond laser pulses. Figure 18(a) shows an OH fragment excitation spectrum recorded by picosecond PFLIF at a pump-probe delay time of 0.5 ns, where it should be borne in mind that the natural OH radical signal has been subtracted. Previous work by Sinha et al. shows that almost none (1.7%) of the available excess energy available after 220 nm photolysis of HO_2 is transferred into vibrational and rotational energy in the OH fragments [89]. Thus, the nascent OH fragments are vibrationally and rotationally cold. An excitation spectrum based on the nascent rotational population distribution as measured by Sinha et al. was simulated and compared to our spectrum; see Figure 18(b). Overall, the two spectra have similar shapes, which

indicate that the OH fragment signal obtained most likely stem from HO_2. The minor differences that are present correspond to somewhat different dissociation wavelengths (266 nm in our study and 220 nm in Sinha et al.) and the fact that our spectrum is acquired under conditions of a 0.5 ns pump-probe delay time, during which time certain rotational relaxation presumably occurred.

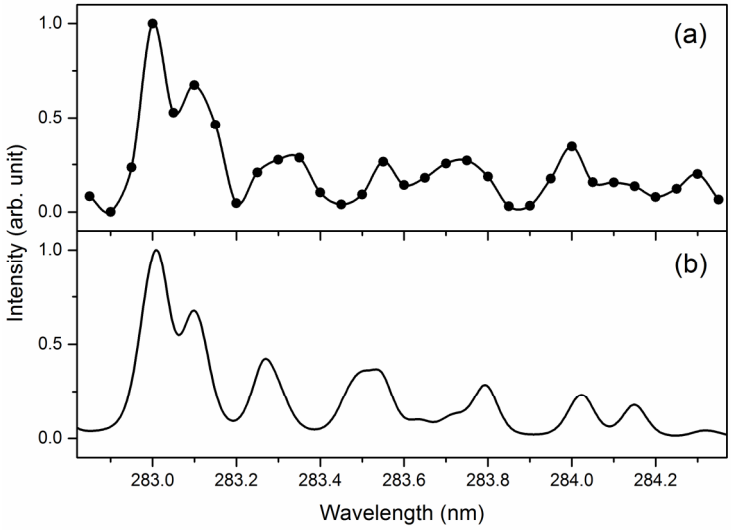

Figure 18(a) An OH fragment excitation spectrum recorded in the reaction zone of a methane/air flame with use of ps-PFLIF with a 0.5 ns pump-probe delay time. (b) A simulated OH fragment excitation spectrum based on the nascent rotational distribution as measured for the 220-nm photolysis of HO_2 by Sinha et al. [89].

5.2 Analysis of the OH-fragment signal in the reaction zone

In the work presented in Paper IV, it was found that the major part of the OH-fragment signal in the reaction zone stems from HO_2, a result also validated in terms of excitation spectra in the work presented in Paper V (see Figure 18). In addition to OH fragments, the photodissociation of HO_2 produces an equal number of oxygen atoms, i.e. $HO_2 + h\nu \rightarrow OH + O$. The oxygen atoms can be created either in their ^3P ground state or in the excited ^1D state. A previous study showed that about 87% of the oxygen atoms are formed in the ^1D state after 220-nm photolysis [89]. Lee et al. also concluded that the UV photolysis of HO_2 produces primarily oxygen atoms in the ^1D state [90]. In order to gain an understanding of the origin of the increasing number of OH-fragment signals produced with an increase in the pump-probe delay time, pump-probe delay studies using picosecond and nanosecond laser pulses were conducted. In addition to the experiments, an analytical expression of the OH

production in the reaction zone based on chemical reactions of $O(^3P)$ and $O(^1D)$ being involved, was derived; see Paper V.

The model employed here for photochemical OH production in the reaction zone of a methane/air flame is described in detail in Paper V. In general, the oxygen atom, dissociated from HO_2, reacts with CH_4 and H_2O to create OH radicals. It is found on the basis of the Konnov C/H/N/O mechanism [29] that the concentrations of CH_4 and H_2O are around three orders of magnitude higher than the concentration of HO_2, this meaning that the chemical reactions that create OH can be dealt with by use of pseudo-first-order kinetics. The full expression for the photochemical OH production that occurs in the reaction zone includes both OH that have been formed directly from $O(^3P)$ and $O(^1D)$ reactions, and OH production through $O(^3P)$ that has been formed via the deactivation of $O(^1D)$. The full expression for OH production as a function of time, *t*, with the insertion of rate constants is:

$$\frac{[OH](t)}{[OH]_0} = (1-x)\left(2-e^{-k_{eff}^{P}t}\right) + x\left\{\left[1+\frac{k_0^D}{k_{eff}^D}\left(1-e^{-k_{eff}^{D}t}\right)\right] + \frac{k'}{k_{eff}^D}\left(1-e^{-k_{eff}^{D}t}\right)\left(1-e^{-k_2^{'}t}\right)\right\} \quad (12)$$

where $[OH]_0$ is the initial OH concentration, and the reaction rate constants involved being defined and listed in Table 1 in Paper V. The variable x ($0 \leq x \geq 1$) is introduced to define the $O(^1D)/O(^3P)$ branching ratio, where $x = 0$ corresponds to 0% $O(^1D)$ and 100% $O(^3P)$, and $x = 1$ corresponds to 100% $O(^1D)$ and 0% $O(^3P)$. The consumption of OH has been neglected in this model, since we are interested in the early buildup time (<200 ns), and during this brief period of time, the OH consumption is less than 13%.

To study the OH-fragment signal in the reaction zone, the peak intensity was extracted for several pump-probe delays, as presented in Figure 19. For short pump-probe delays (<10 ns), picosecond pulses were used, and for longer delays nanosecond pulses were employed. It is important to bear in mind that in both cases the photodissociation process is performed with use of the same laser wavelength but that the picosecond laser pulse has a two orders of magnitude higher photolysis laser intensity than the nanosecond pulse does. It can be clearly seen that the signal strength shown in Figure 19(a), obtained with the use of ps-PFLIF, increases with increasing pump-probe delay. The signal-growth rate is highest initially and then decreases with increasing delay. From the excitation spectrum shown in Figure 18 it can be seen that the rotational population distribution of the OH fragments is non-thermal. Although on the basis of the population transfer that takes place, the signal growth observed at time delays shorter than 5 ns could be expected to be not more than 20%. It can be seen in Figure 19(a) that the signal increase, that occurs is clearly much larger than this, a matter that will soon be explained. Moreover, at nanosecond excitation the OH signal increases with increasing pump-probe delay, as can be seen in Figure 19(b), yet there is no sign of an initial steep gradient, a matter that could, in

principle, be due to the fact that there are no data points for pump-probe delays shorter than 10 ns. The explanation for the observed signal increase in both studies can be due to the OH production that occurs through the oxygen atom reacting with H_2O and CH_4.

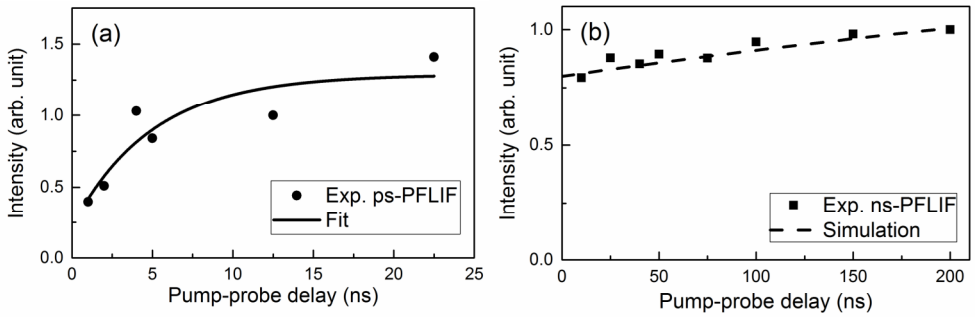

Figure 19 Reaction-zone signal intensities vs pump-probe delay as measured on the basis of (a) picosecond pulses [91] and (b) nanosecond pulses [30]. The symbols represent the measurement data obtained, the solid line in (a) being the fit of the data to the experiments, and the dashed line in (b) being the OH production as simulated on the basis of Equation 12, whereas $x = 0$ and $[OH]_0 = 0.8$.

OH-production curves for different $O(^1D)/O(^3P)$ branching ratios were calculated using Equation 12 and then plotted in Figure 20. The amount of oxygen produced, both in the ground state and in the excited state, by nanosecond and picosecond photodissociation, respectively could then be estimated by comparing the experimental data with the calculated production curves. The results obtained suggest that in the case of picosecond excitation around 60 % of the oxygen atoms are formed in the excited ^1D state, whereas the nanosecond laser pulses do not result in any observed $O(^1D)$ production. It was found that the presence of $O(^1D)$ is manifested mainly in terms of a steep initial slope in the OH production curve. This is shown as a clearly perceptible signal enhancement within the reaction zone by a signal enhancement brought about by photochemically-produced OH that has been created from reactions with the highly reactive $O(^1D)$. The result from the calculation suggests that after about 10 ns, a 40% signal increase is observed in the reaction zone with picosecond pulses. In the case of nanosecond excitation, the signal contribution due to photochemically produced OH was found to be only 1.5% higher than the nascent OH-fragment concentration present in connection with a pump-probe delay of 10 ns. A likely explanation of the difference in the results obtained for picosecond as compared with nanosecond excitation when PFLIF is used, is that picosecond pulses cause two-photon photodissociation of HO_2, this enables $O(^1D)$ to be produced.

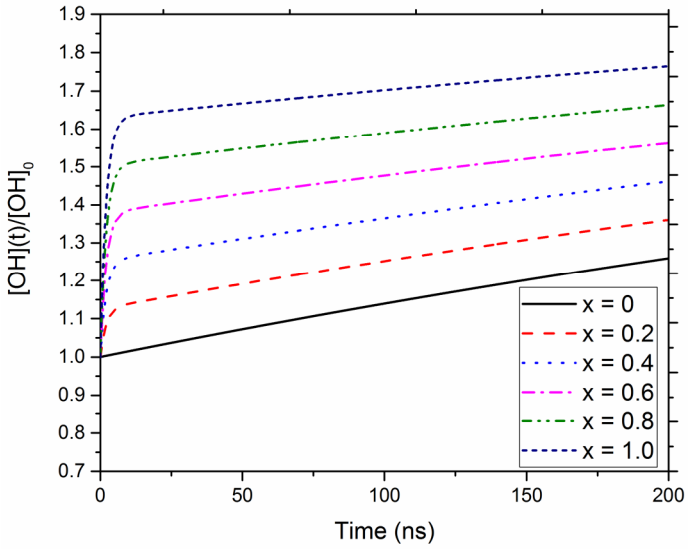

Figure 20 OH production calculated using Equation 12 for various $O(^1D)/O(^3P)$ branching ratios x (where x = 0 means 100% $O(^3P)$ and x = 1 means 100% $O(^1D)$).

5.3 Analysis of the OH-fragment signal in the product zone

From detailed studies carried out in flames of different types (see Paper IV) it was found that the OH signals in the product zone of the methane/air flame, as shown in Figure 17(b), arise due to the photodissociation of hot CO_2. As a first-order approximation, it was assumed that the only production channel at 266 nm is $CO_2 + h\nu \rightarrow CO + O$, where the oxygen atom reacts with H_2O or H_2 to form OH; i.e. $O + H_2O \rightarrow OH + OH$ and $O + H_2 \rightarrow OH + H$. It was found, from pump-probe delay studies using nanosecond pulses, that the chemistry behind OH formation of this sort occurs on a nanosecond time scale and that the signal increases with increasing pump-probe delay, up to a delay of ~1000 ns, at which point the signal starts then to decrease with increasing delay (see Figure 10(a) in Paper IV). In line with this, it can be concluded that picosecond laser pulses potentially allow for a strong suppression of the photochemical interference from CO_2 since the pump-probe delay can be made extremely short, and ultimately be set by the laser pulse duration (80 ps in this case). In Figure 21, the product-zone signal induced by nanosecond and picosecond pulses is plotted versus various pump-probe delay times. The symbols represent experimental results, whereas the solid line is an OH production curve in which it is assumed that 10% of the CO_2 molecules are photodissociated into CO and $O(^3P)$ (see Paper IV for a full account of the calculations [30]). The results obtained show that it is possible to virtually eliminate the product-zone signal interference by using picosecond pulses

and a pump-probe delay time shorter than 4 ns, and this is clearly seen in Figure 5 in Paper V.

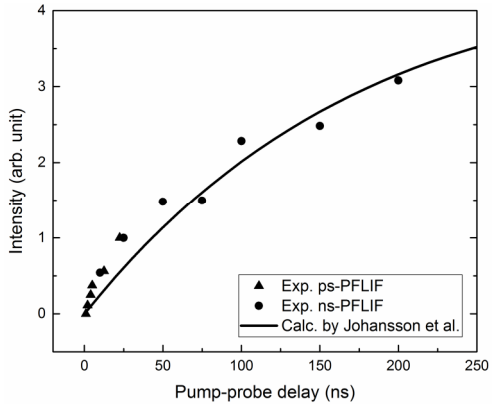

Figure 21 Product-zone signals vs pump-probe delay. The triangles represent the data recorded for picosecond pulses [91], whereas the dots represent experimental data recorded with use of nanosecond pulses, the solid line being chemical-kinetics calculations of the OH production [30].

In addition, a calculation of the amount of OH fragments produced through photodissociation of HO_2 and CO_2 in the methane/air flame, shows that the interfering signal in the product zone can potentially be eliminated, since the number density, N_{di}, of the OH-fragments resulting from the dissociation of species i is strongly dependent on the laser sheet area and the pump pulse energy in the focal volume. The amount of OH fragments from the two separate species can be investigated theoretically by varying the laser pulse energy and the laser sheet area in Equation 10. For 266-nm single-photon excitation, the quantum yield for OH production is 1 for both molecules. The number density of the parent species, CO_2 and HO_2, in the flame that is investigated is calculated on the basis of the Konnov mechanism [29, 30]. The temperature-dependent absorption cross-section of HO_2 is determined using the model reported in [31], where the temperature profile is taken from Paper IV [30]. The absorption cross-section for CO_2 is determined from the model of Jeffries et al. [92]. CO_2 is assumed to be present in the product zone in the flame, in which the temperature is about 2050 K, the absorption cross-section at this temperature is calculated to be $6.01 \cdot 10^{-21}$ cm^2 at 266 nm.

Calculated dissociation ratios, (N_{di}/N_i) for CO_2 and for HO_2, as a function of both laser sheet area and pump pulse energy, are presented in Figure 22(a). The solid lines, showing the dissociation ratio for HO_2, can be seen to reach saturation at appreciably lower laser energy levels than the dissociation ratio of CO_2 (the dashed lines) for the same laser sheet area. On the basis of these results, one can note that when the dissociation processes in HO_2 reach saturation, higher laser pulse energies would then only increase the OH-fragment interference produced in the product zone by hot

CO_2. To investigate the possibility of maximizing the OH-fragment signal in the reaction zone while minimizing the chemically-produced interfering signal in the product zone, the ratio of OH fragments stemming from HO_2 to those originating from CO_2 was calculated for different laser sheet areas and energies, as shown in Figure 22(b). Here, the difference in number density for HO_2 (~$7{\cdot}10^{14}$ cm^3) as compared with CO_2 (~$3{\cdot}10^{17}$ cm^3) was accounted for. The ratio ($N_{OH}(HO_2)/N_{OH}(CO_2)$) should be as high as possible but is limited by the absolute OH-fragment signal strength provided by the HO_2 radicals. Accordingly, minimizing the CO_2-induced interference is a trade-off between minimizing this ratio and maintaining a sufficiently high signal-to-noise ratio for the HO_2 signal (i.e. the OH fragment signal from HO_2). A larger laser sheet area yields a higher ratio but the fluorescence signal level then will be lower than for smaller areas since a lesser number of HO_2 radicals will be dissociated.

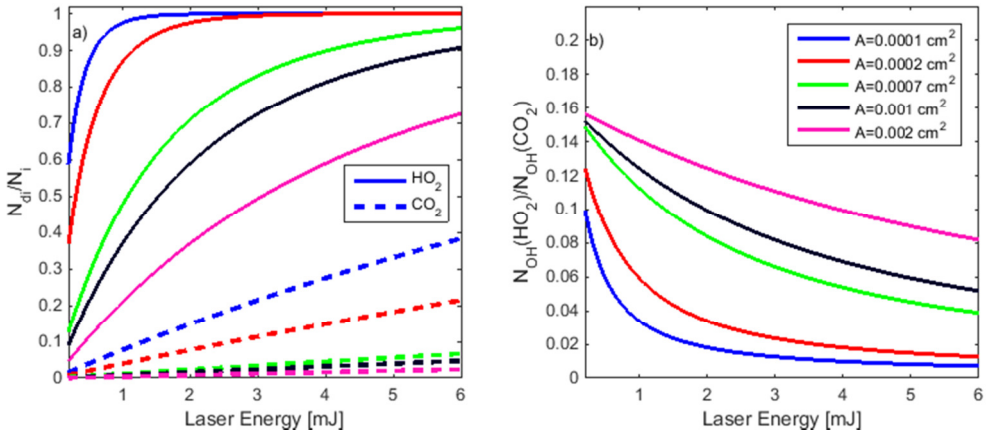

Figure 22(a) The ratio of N_{di}, the photofragments produced, to N_i, the amount of the parent species, where HO_2 is presented as solid lines and CO_2 as dashed lines. The colors represent different laser sheet areas, as indicated in the legend of (b). (b) The ratio of the amount of OH fragments dissociated from the two parent species HO_2 and CO_2.

5.4 Structured illuminated PFLIF for the reduction of natural OH in a CH_4/air flame

In order to overcome the problem of the strong signal interference from naturally existing OH radicals, which overlap spatially with the signal created by the OH fragments, nanosecond PFLIF was combined with structured illumination (Paper VI). Structured illumination (SI) is a method used primarily in microscopy imaging, where is removes out-of-focus signal contributions [93]. For combustion applications, the technique has been used mostly so far for the suppression of multiple scattering in

laser imaging studies of turbid spray systems [94], a detailed account of the technique being found in a PhD thesis by E. Kristensson [95]. In the present case, SI is used to give the OH fragments a recognizable signature through intensity modulating the pump sheet by sending it through a metal transmission grating having a 0.3 mm line separation. This unique signature will have a well-defined spatial frequency that permits the removal of unwanted signals in a post-processing routine termed spatial frequency lock-in (SFLI), in which unwanted signals that have different frequencies than the modulation frequency-encoded pump sheet are suppressed. Parallels of this technique can be seen in lock-in detection and digital-wavelength-modulation spectroscopy dWMS [96]. Through combining PFLIF with SI and using SFLI as the evaluation method, the OH-fragment signal can be distinguished from the naturally present OH signal. Hence, the acquisition of two images, PFLIF and LIF, is no longer a requirement for hydrogen peroxides imaging in flames.

Figure 23, which serve to clarify the use of the SFLI routine, shows in panel (a) an accumulated PFLIF image, I_{RAW}, recorded using an intensity-modulated pump-laser sheet in a CH_4/air flame. The majority of the signal comes from naturally present OH radicals, as is the case for the PFLIF image shown in Figure 17(a). In the evaluation routine, a circular Gaussian window is first applied to the image to remove sharp edges that otherwise produce artifacts in the post-processing routine. The raw image, I_{RAW}, is then Fourier transformed into the frequency plane, $\mathcal{F}(I_{RAW})$, and Figure 23(b) shows the resulting image of the frequency plane. The first harmonic of the modulated signal, indicated by the circles, can be seen on both sides of the origin. As can be noted, the intensity of the higher harmonics decreases rapidly when the harmonic order increases. Both the camera noise and the probe laser beam profile can be viewed here as they cross the origin diagonally in relation to the modulation frequency. The frequencies of the camera noise and the probe beam profile have different angles in the $\mathcal{F}(I_{RAW})$ image, since they are tilted in relation to the horizontal pump beam present in the experimental setup. As a third step, unwanted background interference is extracted by use of an inverted band-pass filter, indicated by the white circles in $\mathcal{F}(I_{RAW})$, that suppresses the modulation frequency. Inverse transformation of this modified I_{RAW} image results in an image that only contains information concerning the background, I_{BKG} (see Figure 23(c)). In a manner, similar to that of the traditional PFLIF-evaluation method, the background image, I_{BKG}, has an appearance similar to that of the LIF image.

A self-compensated image, I_{SC}, is generated as a fourth step through dividing the raw image by the background image, $I_{SC}=I_{RAW}/I_{BKG}$. Here the strong signal interference stemming from the naturally present OH is reduced, whereas the modulated signal is enhanced (see Figure 23(d)). Thereafter, I_{SC} is Fourier transformed into $\mathcal{F}(I_{IC})$ as shown in Figure 23(e), here it is seen that the unwanted frequencies are removed. To extract the frequency-modulated signal and remove any undesirable interferences that remains, a band-pass filter orientated toward the desired harmonic (see the white ellipse that indicates the frequencies of interest) is multiplied by $\mathcal{F}(I_{IC})$. In the final

step, the band-pass-filtered signal is frequency shifted to the origin and is inversely Fourier transformed, and the final image, I_{PFLIF}, are displayed in Figure 23(f). Note that all the images in Figure 23 are extracted from I_{RAW}.

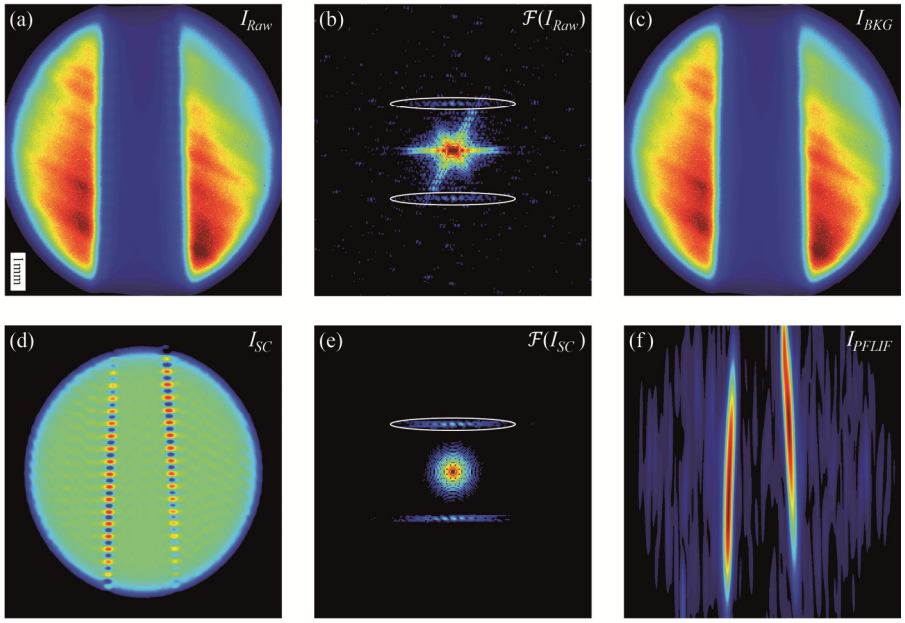

Figure 23(a) PFLIF image, I_{RAW}. (b) The Fourier transform of I_{RAW}, $F(I_{RAW})$, the first harmonic being indicated. (c) I_{BKG}, which is the background-extracted from I_{RAW}. (d) The ratio image, I_{SC}, of I_{RAW} to I_{BKG}. (e) $F(I_{SC})$, the Fourier transform of I_{SC}, the first harmonic of the modulated signal being indicated by a white ellipse. (f) The final OH-photofragment image, I_{PFLIF}.

Figure 23 shows that the OH-fragment signal can be discriminated from the strongly overlapping interfering background signal from the naturally present OH, by having he pump-laser sheet modulated with a well-defined frequency and by using the SFLI evaluation routine. In the work presented in Paper VI, the method is applied to 300 single-shot images recorded in a stoichiometric CH_4/air flame on a coaxial burner. Figure 24(a) shows a typical single-shot image, I_{RAW}, collected by PFLIF that has an intensity-modulated pump-laser sheet. The OH-fragment signal, I_{PFLIF}, which is extracted is presented in Figure 24(b). The mean value of a 2 mm vertical cross section of the I_{RAW} and I_{PFLIF} signals of the 300 single-shots images is shown as the red and the thick blue line, respectively, in Figure 24(c). The grey region around the blue line represents the standard deviation of the I_{PFLIF} signal of the 300 single-shots. A 2 mm vertical cross section of the single-shot PFLLIF image shown in Figure 24(a) is displayed as the red line in (d), clearly showing how the signal of the OH fragments is embedded in the fluorescence profile of the naturally present OH radicals. In Figure 24(d) a 2 mm vertical cross section of I_{PFLIF} is shown as the blue line there, the

previously unrecognized signal from HO_2 are now clearly visible. As can likewise be seen in Figure 24(d), the background signal has been suppressed by a factor of about 50, these results in an increase in the signal-to-interference ratio by a factor of about 20. This shows that the method has the potential of performing single-shot imaging of hydrogen peroxides in non-stationary environments.

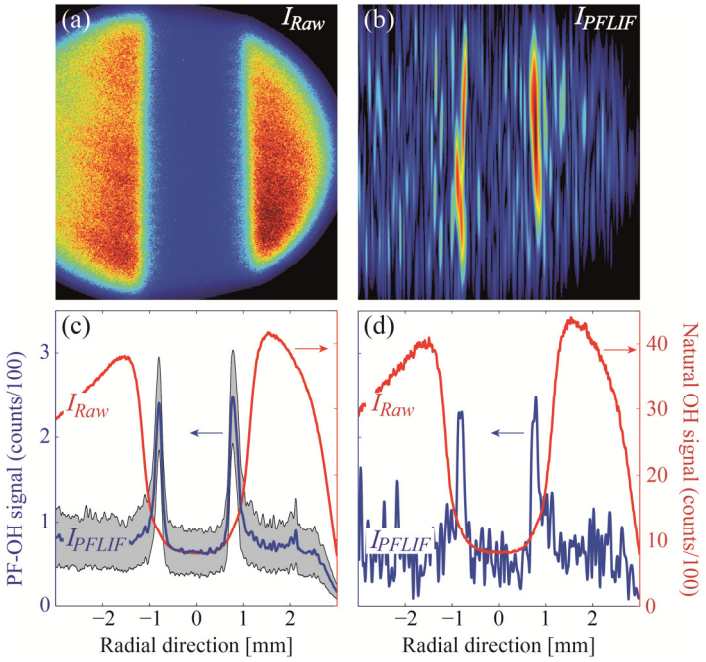

Figure 24(a) A typical single-shot image, I_{RAW}, collected by PFLIF having a modulated pump-laser sheet. (b) An OH-fragment image, I_{PFLIF}, that has been extracted from I_{RAW}. (c) A 2 mm vertical cross section of the mean values of 300 single-shots of I_{RAW} (red line) and I_{PFLIF} (blue line) images, the standard deviation of I_{PFLIF} is presented as the grey area. (d) A 2 mm vertical cross section of I_{RAW} and of I_{PFLIF}, displayed as a red and as a blue line, respectively.

The final image has a spatial resolution of 2 mm in the vertical direction and 0.1 mm in the horizontal direction. The spatial resolution is limited in the final image, since it is defined by the size of the band-pass filter used in the SFLI routine. Although a larger band-pass filter in the Fourier plane provides a higher spatial resolution, the signal-to-noise ratio of the final image would then decreases. A solution to this dilemma is to use a grating having a higher modulation frequency. The frequencies of interest would then appear further away from the origin in the Fourier plane, this making it easier to separate the frequencies of interest from the unwanted interfering signals that contain other frequencies, this in turn allowing the band-pass filter to be larger in size in the vertical direction. Another solution is to use a probe-laser pulse having a more uniform spatial profile, a pulse that does not contain frequencies close to the spatial modulation frequency that is employed.

6 PFLIF employed in an HCCI engine

In the work described in Papers VII-IX, PFLIF was employed for the first time for quantitative one- and two-dimensional crank-angle-resolved concentration measurements of H_2O_2, and of two-dimensional OH temperature distributions in an HCCI engine. Roughly speaking, combustion in an HCCI engine involves a mixture of premixed combustion, typical of spark-ignition engines, and compression ignition, used in diesel engines. In HCCI combustion, autoignition occurs ideally simultaneously at multiple locations within the cylinder, and is controlled by the thermal decomposition of H_2O_2 [97]. The key reactions that lead to the decomposition of H_2O_2 and HO_2 occur at temperatures between 850 and 1200 K [83], and are therefore strongly dependent upon the local pressures and temperatures within the cylinder. Important advantages of HCCI combustion are the high level of efficiency and the low degree of pollutant emission, a significant issue with the technique is the uncontrolled auto-ignition process. H_2O_2 was measured previously in an engine with wavelength-agile absorption spectroscopy [98], a technique restricted to measurement volumes in which variations in temperature along the line of sight are insignificant. In order to better understand and control the autoignition process, and thus gain insight into how to control combustion in HCCI engines, it is highly important to perform two-dimensional in-cylinder quantitative concentration measurements of H_2O_2 as well as to determine in-cylinder temperature distributions.

6.1 Quantitative 1-D H_2O_2 concentration measurements

A two-laser (266-nm pump and ~282.9-nm probe) PFLIF experimental setup was used in an optical 2.0-liter, four-cylinder Toyota D4D diesel engine running under lean conditions (ϕ = 0.26). Further information regarding details of the engine involved are to be found in Paper VII. To verify that the measured PFLIF signal indeed originated from OH and to identify a suitable transition for the probe laser in the measurements that then followed, an excitation spectrum at -23 crank-angle degree (CAD) was obtained. A comparison with simulated OH-LIF excitation spectra generated in LIFBASE [52] confirmed that the signal collected indeed originated from OH. In addition, a pump-probe delay study was performed at the same CAD so as to determine a suitable pump-probe delay time for the measurements to be undertaken. On the basis of these studies, the $Q_1(6)$ transition of the OH (1,0) band was selected, together with a pump-probe delay time of 20 ns, which was short

enough to maintain a strong signal, despite the rapid OH chemistry that was revealed in the pump-probe delay study.

Qualitative one-dimensional crank-angle-resolved measurements of H_2O_2 and of naturally present OH, were performed in a way similar to that employed in the work presented in Paper IV. However, for each CAD three different signals (PFLIF, OH-LIF and OH off-line) were acquired (Paper VII, Figure 4), by a horizontal laser sheet being positioned in the upper part of the cylinder. The strength of the induced H_2O_2 signal was extracted by subtracting the OH-LIF signal from the PFLIF signal. As expected, the hydrogen peroxide signal was found in a temporal regime in which the temperature was below ~1200 K, i.e. between approximately -25 and 0 CAD, see the black squares in Figure 25. The naturally present OH signal was obtained by subtracting the off-line signal from the OH-LIF signal. The onset of the signal from the natural OH took place while the H_2O_2 signal was about to cease, i.e. slightly beyond 0 CAD (top-dead-center, TDC), where the in-cylinder pressure and temperature are sufficiently high for ignition to start. There is a non-zero background for the OH signal found between -30 and -5 CAD (Paper IV, Figure 4), which most likely stems from OH photofragments produced and excited by the probe laser itself. These results verify that H_2O_2 is a precursor to OH, since it is present in a temporal window (~30 CAD wide) preceding the production of OH radicals.

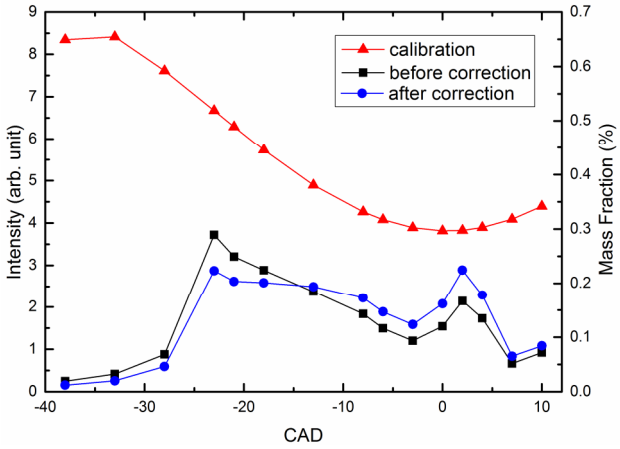

Figure 25 Experimental results from the calibration procedure applied to the H_2O_2 signal. The red triangles show the calibration curve, which corresponds to a constant mass fraction of 0.4%. The black squares indicate the H_2O_2 signal at different CAD values prior to calibration. The blue circles, finally, represent quantitative H_2O_2 mass fractions (coupled to the vertical axis at the right).

In order to convert the one-dimensional H_2O_2 signal intensities into quantitative mass fractions, an in-situ calibration procedure was carried out. The fuel was replaced by an H_2O_2 solution containing 7.6 wt-% H_2O_2 in water, which was vaporized,

mixed with hot air, and injected into the engine cylinder. In the PFLIF calibration measurements, the engine was operated in the same way as during the measurements with the fuel in the tank, and the H_2O_2 mass fraction being assumed to be constant at 0.4%, regardless of CAD. The calibration curve (red triangles) and the resulting quantitative H_2O_2 mass fraction curve (blue circles) are shown in Figure 25. As can be seen, the calibration curve varies with CAD. This is a result of the change in OH fluorescence quantum yield due to variations in quenching, to the pressure broadening of the OH absorption line, as well as, to a minor extent, changes in the population at the rotational level used for excitation, i.e. J'' = 6.5 ($^2\Pi_{3/2}$). The quantitative H_2O_2 mass fraction profile (blue circles) was obtained by dividing the uncorrected curve (black squares) by the calibration curve and multiplying this by 0.4.

To investigate how much of the OH photofragment signal that is due to dissociation of H_2O_2 and HO_2 respectively, the experimental data (blue circles) were compared with H_2O_2 (black dashed line) and HO_2 (red dotted line) concentration profiles being simulated with the software Digital Analysis of Reaction System (DARS), as shown in Figure 26. There is close agreement between the simulated H_2O_2 concentration profiles and the experimental data, regarding the overall concentration level as well as the temporal position and the extent, whereas there are differences between the shapes of the two profiles. The experimental curve shows two peaks, at -23 and +2 CAD, while the simulated H_2O_2 profile has almost a top-hat shape. The two peaks, observed in the experimental curve, probably arise from OH photofragments that stem from HO_2, since the simulated HO_2 curve predicts peaks roughly at the same CADs.

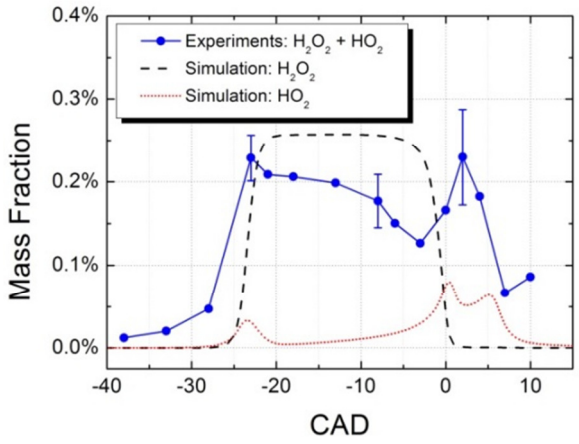

Figure 26 Comparisons of measured mass fractions of hydrogen peroxides (blue circles) with simulated concentration profiles of H_2O_2 (black dashed line) and HO_2 (red dotted line) at different CADs. The error bars correspond to one standard deviation based on 100 single-shot measurements at -23, -8, and +2 CAD, respectively.

As already mentioned, it is not possible with the current PFLIF setup to distinguish H_2O_2 from HO_2. However, the contribution of HO_2 to the total signal can be estimated using the simulated concentrations. The ratios of the concentrations of HO_2-generated to the H_2O_2-generated OH fragments can be expressed as [99],

$$\frac{N_{di-\mathrm{OH/HO_2}}}{N_{di-\mathrm{OH/H_2O_2}}} = \frac{N_{\mathrm{HO2}}}{N_{\mathrm{H_2O_2}}} \cdot \frac{\phi_{\mathrm{OH/HO_2}}}{\phi_{\mathrm{OH/H_2O_2}}} \cdot \frac{F \cdot \sigma_{\mathrm{HO_2}}(T)/hv}{F \cdot \sigma_{\mathrm{H_2O_2}}(T)/hv}. \tag{13}$$

This expression is derived from Equation 10, all of the constants of which, except for the pump laser fluence, F, and the photon energy, hv, have been explained earlier. The ratio $N_{\mathrm{HO2}}/N_{\mathrm{H2O2}}$ is determined on the basis of the two concentration curves given by the DARS simulation shown in Figure 26. The ratio of ϕ_{HO2} to ϕ_{H2O2} is assumed to be 0.5, F and hv cancelling out, the ratio of the HO_2 to the H_2O_2 absorption cross sections being calculated to be ~3 for 600-1100 K [30, 31, 100]. On the basis of this calculation, it is found that HO_2 contributes with 30% to the PFLIF signal at the peak located close to -23 CAD, and that it dominates the signal at the peak close to +2 CAD. However, in general the HO_2 concentration is approximately ten times lower than the H_2O_2 concentration, except in the regions of the two peaks. Thus, the experimental data should, to a large extent, represent a reliable measure of the H_2O_2 concentration.

6.2 Quantitative 2-D H_2O_2 concentration measurements

For two-dimensional quantitative imaging of mainly H_2O_2 in the HCCI engine (Paper VIII), the horizontal laser sheets were turned into becoming vertical laser sheets. Single-shot images, PFLIF, OH-LIF and OH off-line, were recorded at different CADs. The signal intensity in each pixel in the raw data images cannot be converted into mass fraction directly, a new data evaluation process thus needing to be developed. First, at each CAD an averaged PFLIF image was generated from the 100 single-shot images obtained, the averaged image at -18 CAD being shown as an example of this in Figure 27(a). The background signal and the potential interference from the naturally present OH were removed from the PFLIF image by subtracting the corresponding averaged OH-LIF image. The averaged OH-LIF image at -18 CAD is shown in Figure 27(b). This image was also corrected in regarding to the influence of the spatial profiles of the two laser sheets. Simulations of the spatial H_2O_2 concentration distribution in the HCCI-engine, revealed that the H_2O_2 concentration should be nearly uniform and free of interference from HO_2 at -18 CAD, which means that the signal variations found in Figure 27(a) should mainly be due to variations in the product of the two laser intensity profiles. For this reason, after noise reduction by a smoothing procedure, this image was used as a laser-reference image, one reflecting the product of the two laser intensity profiles, as is shown in Figure

27(c). As a second step in the evaluation routine, for each CAD the background-compensated PFLIF image was divided by the laser-reference image.

The variations in quenching for each CAD were accounted for as a third step in the evaluation routine. As mentioned, since the shape of the calibration curve is due to variations in quenching, the mass fraction 0.4% was divided by the calibration curve shown in Figure 25. The result obtained was a curve representing the mass fraction percentage per intensity count versus CAD. For each CAD, the image obtained after the second step was multiplied by the intensity corresponding to the current CAD in the quenching compensated calibration curve. In the final step, the signal intensity was converted into mass fraction. The hydrogen peroxide concentration was assumed to be evenly distributed at -18 CAD, the average mass fraction at this CAD was found on the basis of Figure 25 to be 0.20%. This mass fraction value was divided by the mean intensity of the image obtained at -18 CAD after quenching correction had been carried out, this resulting in a conversion factor of 0.0011% of mass fraction per intensity count. Figure 27(d) shows the resulting hydrogen peroxide mass fraction image at -18 CAD. This image shows a very uniform distribution, which is to be expected, since the laser reference image is derived at that CAD. The pixel value in each CAD image, obtained after quenching correction, was multiplied by the conversion factor, various of the results obtained are shown in the left column in Figure 28. At CAD -6, 0 and +4, the piston blocks the lower parts of the laser sheets.

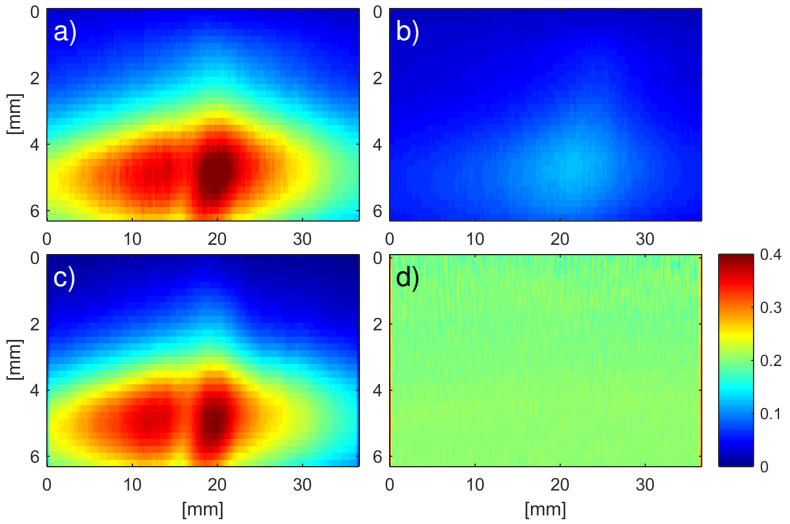

Figure 27(a) A PFLIF image of H_2O_2 at -18 CAD averaged over 100 single shots and (b) the corresponding OH-LIF image. (c) The laser-reference image and (d) the quantitative mass fraction image of H_2O_2 at -18 CAD, the pixel intensity being converted into % mass fraction, as shown in the color bar to the left.

The experimental mass fractions obtained were compared with chemical-kinetics-based simulations, making use of computational fluid dynamics (CFD) and a stochastic reactor model (SRM). Selected two-dimensional experimental and CFD simulated distributions of H_2O_2 and HO_2 at different CADs are presented in Figure 28. These images show a rather close mass fraction level agreement, at the same time that various details of the spatial distribution disagree.

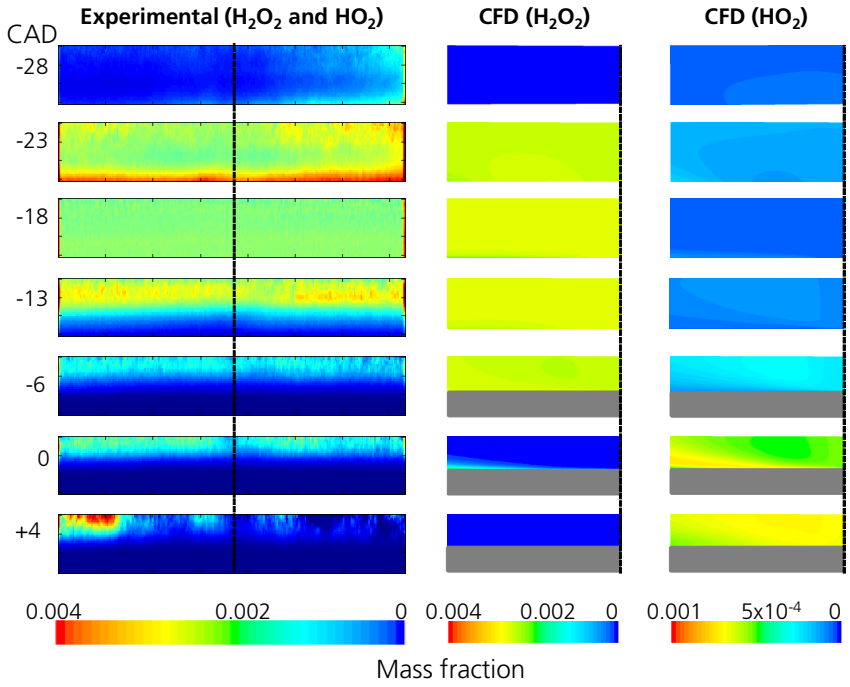

Figure 28 In-cylinder 2D experimental (left) and calculated (center and right column) mass fractions of H_2O_2 and HO_2 at selected CADs. The calculated mass fractions cover half of the measured area indicated by the dashed lines. The solid gray structure represents the piston blocking the laser sheets. The images have a height of 6.2 mm and width of 36.6 mm.

In general, the simulations predict a fairly uniform distribution of the two species, whereas the experimental results show a greater degree of variation of the concentration over the measurement volume. There are several possible reasons for this discrepancy. Actual heterogeneities in the H_2O_2/HO_2 concentration distributions that were not predicted by the model, which is based on completely premixed air/fuel conditions, will make the measured distribution not uniformed. Any spatial temperature variations will affect the strength of the PFLIF signal and be interpreted as concentration variations, and this will be discussed further in the next section. Spatial variations in the laser profile not accounted for in the data processing, and photon noise, could affect the experimental concentrations. Another source of

uncertainty of the experimental results is the reference image used to compensate for the impact of the laser sheet profile. If the image contains any structures due to mass fraction variations within the pass-band of the low-pass filtering, these structures will be interpreted as effects due to variations of the spatial laser profile, which then would impose a systematic error on all images. A systematic error of this sort would appear as islands of high or low mass fractions. However, such systematic "islands" are not observed in the experimental images. Furthermore the strong signal in the upper left hand corner of the experimental image at +4 CAD is most likely due to HO_2, rather than to H_2O_2. It should, be emphasized, however, that the experimental mass fractions in this region should not be interpreted as a quantitative measure of HO_2 concentrations, since the experiments were calibrated against H_2O_2 only.

6.3 Two-dimensional OH temperature measurements

Temperature is one of the key parameters that determine a combustion process, since it affects particle formation, energy release rates, energy transfer, chemical reaction rates, and the overall combustion efficiency [101, 102]. The need of measuring temperatures in different combustion systems with a high degree of spatial and temporal resolution has thus been one of the major driving forces in the development of new diagnostic methods to be conducted in combustion environments. OH-thermometry is a well-established approach that provides the possibility of measuring temperature and relative concentrations simultaneously. With LIF, the OH temperature can be extracted by sensing the population on a multitude of rotational levels, for example by recording and analyzing an excitation spectrum [56, 103-106] or by probing the populations on two rotational states, whose ratio is strongly temperature-dependent [107-111]. A disadvantage of approaches of this sort is that the gas temperature can only be measured when the OH radicals are present in detectable concentrations, which is at temperatures above ~1000 K in combustion environments [112]. In the work presented in Paper IX, the PFLIF technique was used for creating OH fragments within temperature regions in which OH normally is virtually absent, meaning that OH-thermometry becomes applicable in a broad temperature range, between 300 and 2000 K. A clear advantage of creating OH fragments in lower temperature regions (<1200 K) is that the rotational population is far more temperature dependent, making the technique more accurate and sensitive, in this temperature domain

In-cylinder two-dimensional OH temperatures were determined by fitting theoretical OH excitation spectra of different temperatures [52] to experimental spectra recorded in an HCCI-engine. For the experimental spectra, the probe laser was scanned across the $A^2\Sigma^+(v=1)\leftarrow X^2\prod(v=0)$ absorption band in OH. Figure 29(a)-(b) shows the two-dimensional OH temperature distributions recorded at -23 CAD and -13 CAD, respectively, where the corresponding histograms being displayed in Figure 29(c)-(d).

From the experimental results, the mean temperature at -23 CAD is 865 ± 28 K, this corresponding rather closely to 816 K, calculated on the basis of recorded pressure curves. The experimental mean temperature at -13 CAD is 1042 ± 29 K, it differs a bit more from the temperature extracted from measured pressure curves, which is 950 K. This discrepancy is not surprising as the calculation is simply based on the ideal gas law, i.e. no chemistry is included. It is not surprising that the experimental temperature distribution is inhomogeneous, since the corresponding concentration maps measured for -23 CAD and -13 CAD, shown in Figure 28, are clearly inhomogeneous. In HCCI combustion chemistry, at CADs prior to TDC (-25 to 0 CADs), the concentration of H_2O_2 is closely linked to the temperature since the thermal decomposition of H_2O_2 at around 850-1200 K is the chain-branching reaction leading to auto-ignition. Hence, the temperature controls the concentration of H_2O_2 prior to TDC, and in general a high H_2O_2 concentration means a lower temperature, whereas a lower H_2O_2 concentration corresponds to a higher temperature.

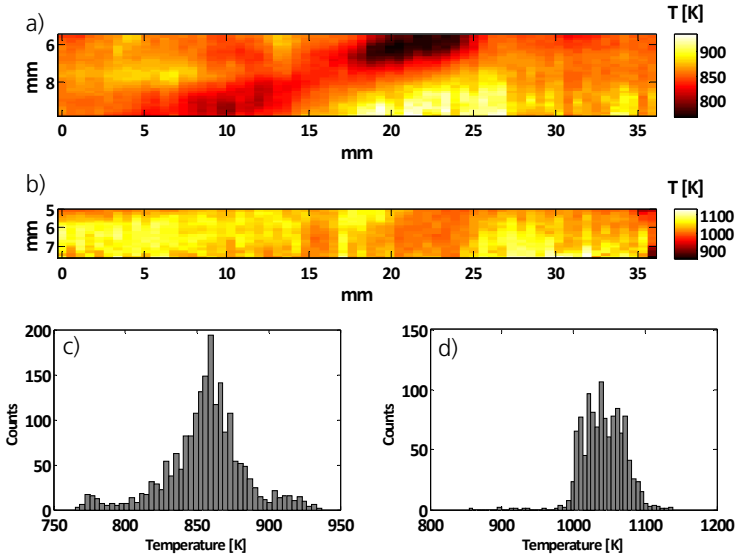

Figure 29 Two-dimensional OH-temperature maps recorded in an HCCI-engine at (a) -23 CAD and (b) -13 CAD, together with corresponding histograms of the OH-temperature distribution at (c) -23 CAD and (d) -13 CAD.

Ideally, the temperature maps at -23 and -13 CAD should be nearly uniform, which is not the case at hand in Figure 29. Plausible explanations are cycle-to-cycle temperature variations or an imperfect fuel/air gas mixture that leads to a non-homogenous distribution of auto-ignition centra. By applying the evaluation method to extract H_2O_2 mass fractions, described in section 6.2, on the single-shot data used for the averaged H_2O_2 mass fraction maps reported in Paper VIII, the H_2O_2 mass

fraction cycle-to-cycle variation could be studied at -23 and -13 CAD. At -23 CAD, noticeable cycle-to-cycle mass fraction variations were found, whereas only minor variations were observed at -13 CAD. This could explain the inhomogeneous temperature maps recorded in the engine, especially at -23 CAD.

It is important to bear in mind that the temperature is evaluated from excitation spectra, in which the laser wavelength is tuned over parts of the $A^2\sum^+(v=1)$-$X^2\prod(v=0)$ absorption band of OH. An excitation spectrum took typically 20 minutes to record, meaning that if the temperature steadily was increasing or decreasing over time, the early part of the spectrum should then correspond to one temperature, whereas the later part of the spectrum should represent another temperature. This is not the case, since it is possible to fit simulated thermal equilibrium spectra to the recorded spectra.

To further develop this technique, a two-line excitation concept should be employed. The temperature would then be extracted from the ratio between the fluorescence signals obtained by probing two rotational levels of OH, whose populations are highly temperature dependent. This opens up the possibility to study the two-dimensional temperature distributions on a single-shot basis, and hence cycle-to-cycle variations of the in-cylinder temperature field.

7 Summary and Outlook

To conclude the work presented in the thesis, primarily two different laser-based measurement techniques towards quantitative species measurements in combustion environments were developed and improved. In the first part of the thesis, the work reported concern the development of a measurement approach for determining fluorescence lifetimes to enable correction of signal losses due to collisional quenching in connection to LIF measurements. In the second part, development of the PFLIF technique for applications in both laboratory flames and an optical engine, aiming at spatially resolved quantitative concentration measurements of H_2O_2 and HO_2, is reported on.

7.1 Towards quantitative laser-induced fluorescence

The possibility of determining fluorescence quantum yields of two species simultaneously is a major step towards being able to measure the quantitative concentrations of two species in one-dimension using LIF (Paper I). The study carried out regarding this emphasizes the importance of measuring fluorescence lifetimes in connection with quenching corrections rather than simply relying on fluorescence lifetime values predicted by models, which can only be done if the concentrations of colliding species are known.

As expressed by Equation 8, there are several parameters that need to be accounted for before the absolute concentrations of the two species can be calculated. In order to correct for the temperature-dependent population at the pumped energy level involved, the Boltzmann factor needs to be determined. This requires information concerning the local temperatures. Such information can be obtained by methods such as coherent anti-Stokes Raman spectroscopy (CARS) or Rayleigh scattering. In order to obtain accurate corrections concerning both the Boltzmann factor, and the lineshape function, it is important that an isolated transition for excitation is selected. A different approach would be to select one or more transitions for which the population is not significantly temperature-dependent. The Boltzmann factor would then have only a minor impact on the results, even if the probe volume passes through a large temperature gradient. In order to deal with the effects of the lineshape function in an accurate way, excitation based on multiple overlapping transitions needs to be avoided. Also in order to obtain accurate corrections for both the

Boltzmann factor and the lineshape function, it is very important to have knowledge about the spatial and temporal profile of the laser pulse.

As mentioned in Chapter 2, the constants in Equation 8 representing the collection and the detection efficiency can be determined through a calibration procedure based on Raman or Rayleigh scattering [8, 12]. Calibration using absorption spectroscopy is yet another possible approach for quantification of LIF [13]. Using the present measurement approach, there can be measurement situations in which calibration of the collection and detection efficiency can be avoided, namely situations in which the concentration of one of the two probed species is known. In such a case, the concentration of the other species can be determined by comparing its fluorescence signal intensities with that of the other species of known concentration. Although, as already discussed, the two signals must be corrected for the fluorescence quantum yield, the Boltzmann factor and the lineshape function. The spectral contents of the two signals must also be rather similar in order for systematic errors in the lens system due to chromatic aberrations, as well as wavelength dependent variations in the sensitivity of the streak camera, to be avoided.

In the work presented in Paper II, a single-camera DIME setup was used to measure toluene fluorescence lifetimes as a function of the oxygen concentration in toluene/nitrogen/oxygen mixtures. DIME opens up the possibility for two-dimensional fluorescence lifetime imaging of the species involved in combustion [44, 45]. In order for single-shot images in non-stationary combustion environments, different approaches can be obtained. Following are two suggestions, one needs to have either a two-camera setup or a scheme in which the fluorescence signal is split into two parts, where one part is being delayed in relation to the other, the two parts are then being imaged on different parts of one camera chip [113]. If DIME is combined with tunable picosecond laser pulse, such as the OPG/OPA system used in the work presented in Paper I, the spectral overlap between the molecular transition and the laser profile can be optimized. This will make the technique applicable for fluorescence lifetime imaging of several different combustion species, such as CH, NO, CO and OH.

7.2 PFLIF - summary and future work

The section that follows summarizes the use of PFLIF for measurements of H_2O_2 and HO_2 in different combustion systems (Papers IV-IX). The work presented in the thesis concerns not only the prompt signal induced by the pump pulse (Paper III) but also photochemically produced OH signals present both in the reaction zone (Paper V) and in the product zone (Paper IV) of a methane/air flame. In the work presented in Paper VI, the problem of interfering signal stemming from OH that is naturally present is solved effectively by combining PFLIF with structured illumination and making use of a spatial lock-in evaluation routine.

On the basis of the work presented in the thesis, the following conclusions regarding the application of PFLIF in a stoichiometric methane/air flame can be drawn:

- The majority (87%) of the OH-fragment signal induced by nanosecond PFLIF is found to stem from HO_2, and 12% of the signal stems from H_2O_2, there is also a minor (<1%) OH fragment signal contribution from CH_3O_2, as chemical kinetic calculations also indicates.
- Problems of prompt fluorescence emission from the reaction zone induced by the pump pulse could be handled by employing a camera gate having a sharp edge. The edge should be positioned in such a way that only fluorescence from OH fragments is recorded. This allows a pump-probe delay time of 10 ns or longer. If the camera gate has a shape resembling the gates used in the present work, a pump-probe delay of around 50 ns is required.
- Pump-probe delay studies with nanosecond and picosecond pulses showed that oxygen atoms produced by HO_2 photolysis were created in different molecular energy states. The states involved were dependent upon the pump laser peak power. In the case of nanosecond excitation, the oxygen was created in its ground state ($O(^3P)$), whereas in the case of picosecond excitation around 60 % of the oxygen atoms created are in the highly reactive excited ^1D state.
- On the basis of the first-order kinetic calculations, assuming that the oxygen atoms from HO_2 only react with CH_4 and H_2O, it could be estimated that the OH signal increase in the reaction zone was produced by the oxygen atoms. For example, at an pump-probe delay time of around 50 ns, there was an OH signal contribution of ~5% from $O(^1D)$ when nanosecond pulses were used, whereas there was ~40% increase in the OH signal contribution when picosecond laser pulses were employed.
- Problems caused by interfering OH signals stemming from hot CO_2 in the product zone of hydrocarbon flames were reduced by use of picosecond laser pulses. It was found on the basis of both calculations and experiments that the chemical reactions creating OH proceed on the nanosecond time scale. This meant that the interfering OH signal could be minimized and almost eliminated when extremely short pump-probe delay times (<5 ns) were employed. Although, nanosecond pulses appear to be favorable for measurements in flames, using pump-probe delay times of 10-50 ns. Under such conditions, the interference from CO_2 could be minimized by the selection of appropriate pump-laser sheet area and pulse energy, resulting in a suppression of the OH signal in the product zone while still having a high enough signal intensity from the OH fragments in the reaction zone.

- When structured illumination is employed for modulating the pump laser sheet, the OH fragments can be given a well-defined spatial frequency that can be discriminated against the overlapping signal from naturally present OH. This can be regarded as an effective and simple way of overcoming the problem of recording two images (PFLIF and LIF). It also provides the possibility for single-shot imaging, which is required in non-stationary environments, such as turbulent flames.
- Regarding the question of whether picosecond or nanosecond pulses should be used for PFLIF diagnostics, both techniques have their limitations, as already alluded to in the points mentioned above. It is important to bear in mind that use of a picosecond laser pulse results in the possibility of multi-photon excitation to occur. This results in lesser insight of the dissociation process and lesser control over it, and possible creation of chemically reactive species, such as $O(^1D)$.

In the work presented in Papers VII-IX, PFLIF was found to be a good tool for measuring in-cylinder quantitative, both one- and two-dimensional, concentrations of H_2O_2 in an HCCI-engine at multiple CADs. Quantitative concentrations were achieved via an on-line calibration procedure in which a known concentration of vaporized H_2O_2 is introduced into the cylinder. It was found that in the region of -22 to 0 CAD, more than 90% of the PFLIF signal stems from H_2O_2, whereas at -23 ± 1 CAD and -2 ± 2 CAD HO_2 appears to be the only significant source of interference. By recording excitation spectrum of the OH-fragments, average two-dimensional temperatures could be obtained at different CADs. The work presented in Papers VII-VIII emphasizes the importance of comparing results of simulations with experimental results. There, H_2O_2 mass fractions at different CADs were compared with simulated concentrations generated by three different tools: DARS, CFD and SRM. Performing comparisons of this type enabled a deeper understanding of the combustion processes, this providing the basis for the development of more adequate combustion models able to serve as more accurate simulation tools. In these studies, it was also shown that simulated concentrations can provide insight into the results obtained experimentally, our finding here indicating at which CADs the H_2O_2 signal is strongly affected by signal contributions from HO_2.

7.2.2 Future work

The PFLIF technique employed here is still far from perfect. A major improvement in the engine study would be to perform the on-line calibration procedure in two-dimensions. Since the distribution of vaporized H_2O_2 is homogenous, the laser-profile can be obtained at any given CAD. The PFLIF image recorded can thus be corrected for a more accurate spatial profile of the two laser pulses than that reported in Paper VIII. Combining PFLIF with structured illumination for two-dimensional H_2O_2

visualization in the HCCI-engine, implies that only the PFLIF image at each CAD needs to be recorded. As was reported in Paper VI, background signal and signal contributions from OH that is naturally present can be removed by the evaluation routine. This opens the way for more accurate single-shot images of H_2O_2 to be obtained near TDC, where OH is created naturally.

Currently, it is not possible to distinguish OH fragments generated by H_2O_2 from fragments originating from HO_2, in either hydrocarbon flames or an HCCI-engine. In this section, various ideas regarding possible approaches for solving this issue in the future will be briefly proposed. It is important to bear in mind that the suggestions given here need to be complemented by a thorough study of the literature before the procedures in question are carried out experimentally.

- It has been found in previous studies that nascent OH fragments created by 193-nm photodissociation of H_2O_2 have a rotational distribution that peaks at the rotational quantum number N = 10 [114]. Sinha et al. [89] have measured the rotational state distribution of OH following 220-nm photodissociation of HO_2. They found that the nascent population is highest in the rotational state N = 1 (J = 1.5) in the F1 branch, that it peaks at N = 3 (J = 2.5) in the F2 branch, and that rotational states above N = 10 are populated to only a negligible degree. From the results found in Paper V, this relationship was confirmed for OH fragments that were generated in a methane/air flame following 266-nm excitation [91]. Through use of picosecond-PFLIF it should in principle be possible to distinguish OH fragments stemming from H_2O_2 from those originating from HO_2, by use of a short pump-probe delay time (<100 ps) and two different probe laser wavelengths. One laser could for example be tuned to probe N = 1 (for HO_2) and the other to N = 10 (H_2O_2). In order to really generate an extremely short pump-probe delay time, the experimental setup could be designed so as to consist of a femtosecond pump pulse and a picosecond probe pulse.
- It was shown here, particularly in the study presented in Paper III, that short laser pulses induce prompt fluorescence from the flame, imposing the restriction that pump-probe delays must be longer than 10 ns. One possible approach of getting around this problem could be to use spatially modulated pump and probe beams, where the modulation frequencies are different. The prompt fluorescence signal would be labeled by one spatial frequency, whereas the OH photofragments would be labeled by a modulated frequency representing a combination of the frequencies from the pump and probe beams. It should be possible in the frequency domain then to distinguish the OH fragment signals from the promptly induced fluorescence signals.
- Taking advantage of the difference between the wavelength dependence of the absorption cross section of HO_2 and H_2O_2, the concentration ratio of the two species could be distinguished by use of two different pump wavelengths.

Figure 30 shows a plot of the ratio of the HO_2 cross section [31] to the H_2O_2 cross section [115] as a function of wavelength for three different temperatures (300, 600 and 1100 K). The idea behind this approach relies on finding two wavelengths where the two cross sections differ considerably. From the figure, it is found that 266 nm generates a ratio of around 3, while 220 nm have a ratio of around 11.5 K. These two wavelengths can easily be generated by current laser systems. The first laser will generate the following signal, $S_{266}=N_{HO2}\cdot\sigma_{HO2}(\lambda_{266})+N_{H2O2}\cdot\sigma_{H2O2}(\lambda_{266})$, whereas the other pump pulse will generate the following signal, $S_{220}=N_{HO2}\cdot\sigma_{HO2}(\lambda_{220})+ N_{H2O2}\cdot\sigma_{H2O2}(\lambda_{220})$. These two equations can simply be solved and the relation between the concentrations of HO_2 to H_2O_2 may be extracted. For such an experiment to be carried out, an achromatic lens would be needed, as well as two different dye-laser systems, one dye-laser to generate the two pump beams that create the OH fragments, and one dye-laser that excite the generated OH radicals. Either two cameras or one camera with a stereoscope would be needed to collect the signal, or alternatively the two pump pulses could be arranged so that they differe in terms of spatial modulation frequency. Again, the PFLIF signals generated by the respective pump pulses would differ in terms of the location in the frequency plane at which they will appear. From Figure 30 it is revealed that the ratio of the cross sections is temperature dependent, this might limit this approach to laminar flames, in which the temperature profile could be determined from CARS or Rayleigh measurements, or to measurements in the HCCI-engine, in which the temperature field is expected to be fairly homogenous.

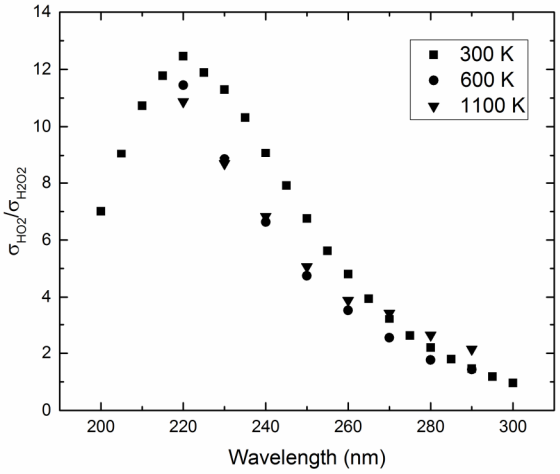

Figure 30 The ratio of the HO_2 absorption cross section to the H_2O_2 cross section as a function of wavelengths at three different temperatures. The different temperatures are indicated by different symbols.

- Finally, another idea for making the technique more species-specific would be to employ two-photon excitation through use of a vibrational state in the ground electronic state, followed by a UV/visible pulse to excite the molecules in the upper vibrational state to their repulsive upper excited state, where they would dissociate into OH. The wavelength of the UV/visible pulse should not have sufficient energy on its own to reach the repulsive state. Rather it should only be able to access the repulsive state under conditions of the IR pulse being tuned to a vibrational state in the molecule. Figure 31 illustrates this approach schematically. Although, the two-photon process should be favored experimentally by the use of picosecond pulses, use of nanosecond pulses would have the advantage of better overlapping the laser profile with the absorption line.

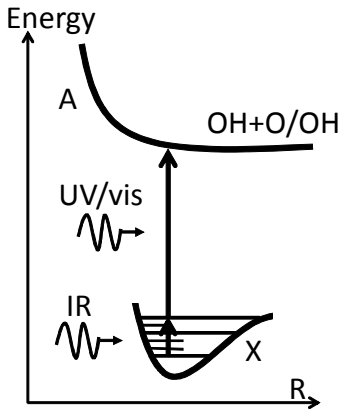

Figure 31 A schematic illustration of the principle of two-photon excitation to a repulsive state in HO_2 or H_2O_2 by use of an IR pulse followed by a UV/visible pulse.

Acknowledgments

I would like to start by thanking my supervisors Joakim Bood and Marcus Aldén for giving me the opportunity to pursue a PhD degree at the division of Combustion Physics. A special thanks to Joakim for inspiring and encouraging me during the daily work in the laboratory and the office. I especially appreciate that you always take the time to explain and to look into the details of the physics. During these five years, I have truly enjoyed all the interesting discussions that we had regarding physics, football and life. Marcus I want to thank you for providing a great place to work at with a friendly and open atmosphere.

I want to give a special acknowledgement to the co-authors of the papers presented in the thesis. The papers would not exist if it was not for you all. It has been a pleasure to work with you all in the laboratory, discussing the results and writing the papers. I have learnt a lot from you and I have had a lot of fun even if the lasers sometimes have worked against us.

I also want to take the opportunity to thank all the colleagues at the division of Combustion Physics. A special thanks to Nils-Erik for being my work-out and traveling buddy, Rikard for being my Matlab guru, Jesper for being my Superhero, Moah for being my power-suite friend, Fahed for being my MasterChef, and Johan S, Emil, Jocke R, Linda, Kajsa, Elin, Andreas E for helping me survive these five years with funny and interesting discussions during lunch, memorable conference trips, and making these five years a memory for life. It has been a privilege to have Eva Åkesson as my mentor for all these years. You are a great inspiration to me, and I am full of energy after our meetings. Jag vill avsluta med att tacka mina vänner och min familj. Tack för att ni alltid har stöttat mig och trott på mig när jag själv har tvivlat, jag hade aldrig kommit hit om det inte varit fösr ert stöd.

Malin Jonsson, October 2015, Lund

References

1. IEA, *Key World Energy Statistics*. 2014. 1-82.
2. Stocker, T., D. Qin, G.-K. Plattner, L. Alexander, S. Allen, N. Bindoff, F.-M. Bréon, J. Church, U. Cubasch, and S. Emori, *Technical summary*, in *Climate Change 2013: The Physical Science Basis. Contribution of Working Group I to the Fifth Assessment Report of the Intergovernmental Panel on Climate Change*. 2013, Cambridge University Press. p. 33-115.
3. WHO., *Air Quality Guidelines: Global Update 2005. Particulate Matter, Ozone, Nitrogen Dioxide and Sulfur Dioxide*. 2006: World Health Organization.
4. Eckbreth, A.C., *Laser diagnostics for combustion temperature and species*. 1996: Combustion science and technology book series. Gordon and Breach Publishers.
5. Kohse-Höinghaus, K. and J.B. Jeffries, *Applied combustion diagnostics*. 2002: Combustion: An international series. Taylor and Francis.
6. Banwell, C.N. and E.M. McCash, *Fundamentals of molecular spectroscopy*. 1994: The McGraw-Hill Companies.
7. Kohse-Höinghaus, K., *Laser techniques for the quantitative detection of reactive intermediates in combustion systems.* Progress in Energy and Combustion Science, 1994. **20**(3): p. 203-279.
8. Luque, J. and D.R. Crosley, *Absolute CH concentrations in low-pressure flames measured with laser-induced fluorescence.* Applied Physics B, 1996. **63**(1): p. 91-98.
9. Piepmeier, E.H., *Theory of laser saturated atomic resonance fluorescence.* Spectrochimica Acta Part B: Atomic Spectroscopy, 1972. **27**(10): p. 431-443.
10. Andresen, P., A. Bath, W. GrÖger, H.W. Lülf, G. Meijer, and J.J.t. Meulen, *Laser-induced fluorescence with tunable excimer lasers as a possible method for instantaneous temperature field measurements at high pressures: checks with an atmospheric flame.* Appl. Opt., 1988. **27**(2): p. 365-378.
11. Cheng, T.S., J.A. Wehrmeyer, R.W. Pitz, O. Jarrett Jr, and G.B. Northam, *Raman measurement of mixing and finite-rate chemistry in a supersonic hydrogen-air diffusion flame.* Combustion and Flame, 1994. **99**(1): p. 157-173.
12. Luque, J., R.J.H. Klein-Douwel, J.B. Jeffries, G.P. Smith, and D.R. Crosley, *Quantitative laser-induced fluorescence of CH in atmospheric pressure flames.* Applied Physics B, 2002. **75**(6-7): p. 779-790.
13. Cheskis, S., *Quantitative measurements of absolute concentrations of intermediate species in flames.* Progress in Energy and Combustion Science, 1999. **25**(3): p. 233-252.
14. Luque, J., P.A. Berg, J.B. Jeffries, G.P. Smith, D.R. Crosley, and J.J. Scherer, *Cavity ring-down absorption and laser-induced fluorescence for quantitative measurements of CH radicals in low-pressure flames.* Applied Physics B, 2004. **78**(1): p. 93-102.

15. Bergano, N.S., P.A. Jaanimagi, M.M. Salour, and J.H. Bechtel, *Picosecond laser-spectroscopy measurement of hydroxyl fluorescence lifetime in flames.* Opt. Lett., 1983. **8**(8): p. 443-445.
16. Rodgers, M.O., K. Asai, and D.D. Davis, *Photofragmentation-laser induced fluorescence: a new method for detecting atmospheric trace gases.* Appl. Opt., 1980. **19**(21): p. 3597-3605.
17. Simeonsson, J.B. and R.C. Sausa, *A Critical Review of Laser Photofragmentation/Fragment Detection Techniques for Gas-Phase Chemical Analysis.* Applied Spectroscopy Reviews, 1996. **31**(1-2): p. 1-72.
18. Simeonsson, J.B. and R.C. Sausa, *Laser photofragmentation/fragment detection techniques for chemical analysis of the gas phase.* TrAC Trends in Analytical Chemistry, 1998. **17**(8–9): p. 542-550.
19. Sandholm, S., J. Olson, J. Bradshaw, R. Talbot, H. Singh, G. Gregory, D. Blake, B. Anderson, G. Sachse, J. Barrick, J. Collins, K. Klemm, B. Lefer, O. Klemm, K. Gorzelska, D. Herlth, and D. O'Hara, *Summertime partitioning and budget of NOy compounds in the troposphere over Alaska and Canada: ABLE 3B.* Journal of Geophysical Research: Atmospheres, 1994. **99**(D1): p. 1837-1861.
20. Schendel, J.S., R.E. Stickel, C.A. van Dijk, S.T. Sandholm, D.D. Davis, and J.D. Bradshaw, *Atmospheric ammonia measurement using a VUV/photo-fragmentation laser-induced fluorescence technique.* Applied optics, 1990. **29**(33): p. 4924-4937.
21. Heflinger, D., T. Arusi-Parpar, Y. Ron, and R. Lavi, *Application of a unique scheme for remote detection of explosives.* Optics Communications, 2002. **204**(1–6): p. 327-331.
22. Hynes, A.J., R.C. Richter, and C.J. Nien, *Laser photofragmention-laser induced fluorescence detection of the hydroperoxyl radical: photofragment energy distributions, detection sensitivity and kinetics.* Chemical Physics Letters, 1996. **258**(5–6): p. 633-638.
23. Okabe, H., *Photochemistry of Small Molecules*. 1978: John Wiley and Sons, New York.
24. Johansson, O., J. Bood, M. Aldén, and U. Lindblad, *Detection of Hydrogen Peroxide Using Photofragmentation Laser-Induced Fluorescence.* Appl. Spectrosc., 2008. **62**(1): p. 66-72.
25. Kulatilaka, W.D., J.H. Frank, B.D. Patterson, and T.B. Settersten, *Analysis of 205-nm photolytic production of atomic hydrogen in methane flames.* Applied Physics B, 2009. **97**(1): p. 227-242.
26. Atkinson, R., D. Baulch, R. Cox, J. Crowley, R. Hampson, R. Hynes, M. Jenkin, M. Rossi, and J. Troe, *Evaluated kinetic and photochemical data for atmospheric chemistry: Volume I-gas phase reactions of O x, HO x, NO x and SO x species.* Atmospheric chemistry and physics, 2004. **4**(6): p. 1461-1738.
27. Ruscic, B., R.E. Pinzon, M.L. Morton, N.K. Srinivasan, M.-C. Su, J.W. Sutherland, and J.V. Michael, *Active Thermochemical Tables: Accurate Enthalpy of Formation of Hydroperoxyl Radical, HO2†.* The Journal of Physical Chemistry A, 2006. **110**(21): p. 6592-6601.

28. Baulch, D.L., R.A. Cox, P.J. Crutzen, R.F. Hampson, J.A. Kerr, J. Troe, and R.T. Watson, *Evaluated Kinetic and Photochemical Data for Atmospheric Chemistry: Supplement I CODATA Task Group on Chemical Kinetics.* Journal of Physical and Chemical Reference Data, 1982. **11**(2): p. 327-496.
29. Konnov, A.A., *Implementation of the NCN pathway of prompt-NO formation in the detailed reaction mechanism.* Combustion and Flame, 2009. **156**(11): p. 2093-2105.
30. Johansson, O., J. Bood, B. Li, A. Ehn, Z.S. Li, Z.W. Sun, M. Jonsson, A.A. Konnov, and M. Aldén, *Photofragmentation laser-induced fluorescence imaging in premixed flames.* Combustion and Flame, 2011. **158**(10): p. 1908-1919.
31. Joens, J.A., *A Model for the Temperature Dependence of the Near UV Absorption Spectra of Organic Peroxy Radicals.* The Journal of Physical Chemistry, 1994. **98**(5): p. 1394-1397.
32. Wellander, R., M. Richter, and M. Aldén, *Time resolved, 3D imaging (4D) of two phase flow at a repetition rate of 1 kHz.* Opt. Express, 2011. **19**(22): p. 21508-21514.
33. Wellander, R., M. Richter, and M. Aldén, *Time-resolved (kHz) 3D imaging of OH PLIF in a flame.* Experiments in Fluids, 2014. **55**(6): p. 1-12.
34. Siegman, A.E., *Lasers*. 1986: University Science Books, Mill Valley, CA.
35. Svanberg, S., *Atmoic and molecular spectroscopy*. 2001: Springer.
36. Ossler, F., J. Larsson, and M. Aldén, *Measurements of the effective lifetime of O atoms in atmospheric premixed flames.* Chemical Physics Letters, 1996. **250**(3–4): p. 287-292.
37. Köllner, M., P. Monkhouse, and J. Wolfrum, *Time-resolved LIF of OH(A 2Σ+, v′=1 and v′=0) in atmospheric-pressure flames using picosecond excitation.* Chemical Physics Letters, 1990. **168**(3–4): p. 355-360.
38. Köllner, M. and P. Monkhouse, *Time-resolved LIF of OH in the flame front of premixed and diffusion flames at atmospheric pressure.* Applied Physics B, 1995. **61**(5): p. 499-503.
39. Agrup, S. and M. Aldén, *Measurements of the collisionally quenched lifetime of CO in hydrocarbon flames.* Applied Spectroscopy, 1994. **48**(9): p. 1118-1124.
40. Di Teodoro, F., J.E. Rehm, R.L. Farrow, and P.H. Paul, *Collisional quenching of CO B [sup 1] Sigma[sup +](v[sup [prime]] = 0) probed by two-photon laser-induced fluorescence using a picosecond laser.* The Journal of Chemical Physics, 2000. **113**(8): p. 3046-3054.
41. Schwarzwald, R., P. Monkhouse, and J. Wolfrum, *Fluorescence lifetimes for nitric oxide in atmospheric pressure flames using picosecond excitation.* Chemical Physics Letters, 1989. **158**(1–2): p. 60-64.
42. Renfro, M.W., A. Chaturvedy, and N.M. Laurendeau, *semi-quantative measurments of CH concentration in atmospheric-pressure counterflow diffusion flames using picosecond laser-induced fluorescence* Combustion Science and Technology, 2001. **169**(1): p. 25-43.
43. Dreizler, A., R. Tadday, P. Monkhouse, and J. Wolfrum, *Time and spatially resolved LIF of OH A 2Σ+(v′=1) in atmospheric-pressure flames using picosecond excitation.* Applied Physics B, 1993. **57**(1): p. 85-87.

44. Ehn, A., O. Johansson, A. Arvidsson, M. Aldén, and J. Bood, *Single-laser shot fluorescence lifetime imaging on the nanosecond timescale using a Dual Image and Modeling Evaluation algorithm.* Opt. Express, 2012. **20**(3): p. 3043-3056.
45. Ehn, A., O. Johansson, J. Bood, A. Arvidsson, B. Li, and M. Aldén, *Fluorescence lifetime imaging in a flame.* Proceedings of the Combustion Institute, 2011. **33**(1): p. 807-813.
46. Kee, R.J., G. Dixon-Lewis, J. Warnatz, M.E. Coltrin, and J.A. Miller, Sandia National Laboratories Report, SAND86-8246, 1990.
47. Kee, R.J., J.F. Grcar, M.D. Smoke, and J.A. Miller, Sandia National Laboratories Report, SAND86-8240, 1990.
48. Kee, R.J., F.M. Rupley, and J.A. Miller, Sandia National Laboratories Report, SAND89-8009, 1990.
49. Lutz, A.E., R.J. Kee, and J.A. Miller, Sandia National Laboratories Report, SAND87-8248, 1990.
50. Smith, G.P., D.M. Golden, M. Frenklach, N.W. Moriarty, Z.B. Eiteneer, M. Goldenberg, T. Bowman, R.K. Hanson, S. Song, W.C. Gardiner, V.V. Lissianski, and Z. Qin, GRI-Mech 3.0. http://www.me.berkeley.edu/gri_mech/.
51. Heard, D.E. and D.A. Henderson, *Quenching of OH (A 2[capital Sigma]+, v[prime or minute]=0) by several collision partners between 200 and 344 K. Cross-section measurements and model comparisons.* Physical Chemistry Chemical Physics, 2000. **2**(1): p. 67-72.
52. Luque, J. and D.R. Crosley. "LIFBASE: Database and spectral simulation (version 1.5)" 1999.
53. Lee, M.P., R. Kienle, and K. Kohse-Höinghaus, *Measurements of rotational energy transfer and quenching in OHA 2 σ +,υ′ = 0 at elevated temperature.* Applied Physics B, 1994. **58**(6): p. 447-457.
54. Kienle, R., M.P. Lee, and K. Kohse-Höinghaus, *A detailed rate equation model for the simulation of energy transfer in OH laser-induced fluorescence.* Applied Physics B, 1996. **62**(6): p. 583-599.
55. Hartlieb, A.T., D. Markus, W. Kreutner, and K. Kohse-Höinghaus, *Measurement of vibrational energy transfer of OH (A2Σ+,v′=1⟶0) in low-pressure flames.* Applied Physics B, 1997. **65**(1): p. 81-91.
56. Bechtel, J.H. and R.E. Teets, *Hydroxyl and its concentration profile in methane-air flames.* Appl. Opt., 1979. **18**(24): p. 4138-4144.
57. Schwarzwald, R., P. Monkhouse, and J. Wolfrum, *Picosecond fluorescence lifetime measurement of the OH radical in an atmospheric pressure flame.* Chemical Physics Letters, 1987. **142**(1–2): p. 15-18.
58. Settersten, T.B., A. Dreizler, and R.L. Farrow, *Temperature- and species-dependent quenching of CO B probed by two-photon laser-induced fluorescence using a picosecond laser.* The Journal of Chemical Physics, 2002. **117**(7): p. 3173-3179.
59. Brackmann, C., J. Sjöholm, J. Rosell, M. Richter, J. Bood, and M. Aldén, *Picosecond excitation for reduction of photolytic effects in two-photon laser-induced fluorescence of CO.* Proceedings of the Combustion Institute, 2013. **34**(2): p. 3541-3548.

60. Bengtsson, P.-E., *Simultaneous Two-Dimensional Visualization of Soot and OH in Flames Using Laser-Induced Fluorescence.* Appl. Spectrosc., 1996. **50**(9): p. 1182-1186.
61. Linow, S., A. Dreizler, J. Janicka, and E.P. Hassel, *Comparison of two-photon excitation schemes for CO detection in flames.* Applied Physics B, 2000. **71**(5): p. 689-696.
62. Tjossem, P.J.H. and K.C. Smyth, *Multiphoton excitation spectroscopy of the B [sup 1] Sigma [sup +] and C [sup 1] Sigma [sup +] Rydberg states of CO.* The Journal of Chemical Physics, 1989. **91**(4): p. 2041-2048.
63. Ehn, A., *Towards quantitative diagnostics using short-pulse laser techniques*. 2012, PhD Thesis, Lund University.
64. Zhou, B., J. Kiefer, J. Zetterberg, Z. Li, and M. Aldén, *Strategy for PLIF single-shot HCO imaging in turbulent methane/air flames.* Combustion and Flame, 2014. **161**(6): p. 1566-1574.
65. Kiefer, J., Z.S. Li, T. Seeger, A. Leipertz, and M. Aldén, *Planar laser-induced fluorescence of HCO for instantaneous flame front imaging in hydrocarbon flames.* Proceedings of the Combustion Institute, 2009. **32**(1): p. 921-928.
66. Sick, V. and N. Wermuth, *Single-shot imaging of OH radicals and simultaneous OH radical/acetone imaging with a tunable Nd : YAG laser.* Applied Physics B, 2004. **79**(2): p. 139-143.
67. Kong, F., Q. Luo, H. Xu, M. Sharifi, D. Song, and S.L. Chin, *Explosive photodissociation of methane induced by ultrafast intense laser.* The Journal of Chemical Physics, 2006. **125**(13): p. 133320.
68. Xu, H.L., J.F. Daigle, Q. Luo, and S.L. Chin, *Femtosecond laser-induced nonlinear spectroscopy for remote sensing of methane.* Applied Physics B, 2006. **82**(4): p. 655-658.
69. Xu, H.L., Y. Kamali, C. Marceau, P.T. Simard, W. Liu, J. Bernhardt, G. Méjean, P. Mathieu, G. Roy, J.-R. Simard, and S.L. Chin, *Simultaneous detection and identification of multigas pollutants using filament-induced nonlinear spectroscopy.* Applied Physics Letters, 2007. **90**(10): p. 101106.
70. Kotzagianni, M. and S. Couris, *Femtosecond laser induced breakdown for combustion diagnostics.* Applied Physics Letters, 2012. **100**(26): p. 264104.
71. Li, H.-L., H.-L. Xu, B.-S. Yang, Q.-D. Chen, T. Zhang, and H.-B. Sun, *Sensing combustion intermediates by femtosecond filament excitation.* Optics Letters, 2013. **38**(8): p. 1250-1252.
72. Kotzagianni, M. and S. Couris, *Femtosecond laser induced breakdown spectroscopy of air–methane mixtures.* Chemical Physics Letters, 2013. **561–562**(0): p. 36-41.
73. Chu, W., H. Li, J. Ni, B. Zeng, J. Yao, H. Zhang, G. Li, C. Jing, H. Xie, H. Xu, K. Yamanouchi, and Y. Cheng, *Lasing action induced by femtosecond laser filamentation in ethanol flame for combustion diagnosis.* Applied Physics Letters, 2014. **104**(9): p. 091106.
74. Western, C.M. PGOPHER, A program for simulating rotational structure, 2010.
75. Ram, R.S. and P.F. Bernath, *Revised molecular constants and term values for the X3Σ− and A3Π states of NH.* Journal of Molecular Spectroscopy, 2010. **260**(2): p. 115-119.

76. Schwarzwald, R., P. Monkhouse, and J. Wolfrum, *Fluorescence studies of OH and CN radicals in atmospheric pressure flames using picosecond excitation.* Symposium (International) on Combustion, 1989. **22**(1): p. 1413-1420.
77. Jonsson, M., J. Borggren, M. Aldén, and J. Bood, *Time-resolved spectroscopic study of photofragment fluorescence in methane/air mixtures and its diagnostic implications.* Applied Physics B, 2015. **120**(4): p. 587-599.
78. Logan, J.A., M.J. Prather, S.C. Wofsy, and M.B. McElroy, *Tropospheric chemistry: A global perspective.* Journal of Geophysical Research: Oceans, 1981. **86**(C8): p. 7210-7254.
79. Lee, M., B.G. Heikes, and D.W. O'Sullivan, *Hydrogen peroxide and organic hydroperoxide in the troposphere: a review.* Atmospheric Environment, 2000. **34**(21): p. 3475-3494.
80. Salooja, K.C., *The degenerate chain braching intermediate in hydrocarbon combustion: Some evidence from studies on the isomeric hexanes.* Combustion and Flame, 1965. **9**(3): p. 219-227.
81. Michael, J.V., J.W. Sutherland, L.B. Harding, and A.F. Wagner, *Initiation in H2/O2: Rate constants for H2+O2→H+HO2 at high temperature.* Proceedings of the Combustion Institute, 2000. **28**(2): p. 1471-1478.
82. Pitz, W.J. and C.K. Westbrook, *Chemical kinetics of the high pressure oxidation of n-butane and its relation to engine knock.* Combustion and Flame, 1986. **63**(1–2): p. 113-133.
83. Westbrook, C.K., *Chemical kinetics of hydrocarbon ignition in practical combustion systems.* Proceedings of the Combustion Institute, 2000. **28**(2): p. 1563-1577.
84. Griffiths, J.F., K.J. Hughes, and R. Porter, *The role and rate of hydrogen peroxide decomposition during hydrocarbon two-stage autoignition.* Proceedings of the Combustion Institute, 2005. **30**(1): p. 1083-1091.
85. Johansson, O., *Development and application of photofragmentation laser-induced fluorescence for visualization of hydrogen peroxides*. 2011, PhD, Thesis, Lund University.
86. L. Hagen, C. and S. T. Sanders, *Investigation of multi-species (H 2 O 2 and H 2 O) sensing and thermometry in an HCCI engine by wavelength-agile absorption spectroscopy.* Measurement Science and Technology, 2007. **18**(7): p. 1992.
87. Hartmann, D., J. Karthaeuser, and R. Zellner, *The 248-nm photofragmentation of the peroxymethyl radical.* The Journal of Physical Chemistry, 1990. **94**(7): p. 2963-2966.
88. Kassner, C., P. Heinrich, F. Stuhl, S. Couris, and S. Haritakis, *Fragments in the UV photolysis of the CH3 and CH3O2 radicals.* Chemical Physics Letters, 1993. **208**(1–2): p. 27-31.
89. Sinha, A., J. Coleman, and R. Barnes, *Photodissociation Dynamics of HO2 at 220 nm: Determination of the O(1D):O(3P) Branching Ratio.* The Journal of Physical Chemistry, 1994. **98**(48): p. 12462-12465.
90. Lee, L.C., *Observation of O(1D) produced from photodissociation of HO2 at 193 and 248 nm.* The Journal of Chemical Physics, 1982. **76**(10): p. 4909-4915.

91. Jonsson, M., K. Larsson, J. Borggren, M. Aldén, and J. Bood, *Investigation of photochemical effects in flame diagnostics with picosecond photofragmentation laser-induced fluorescence.* In manuscript, 2015.
92. Jeffries, J.B., C. Schulz, D.W. Mattison, M.A. Oehlschlaeger, W.G. Bessler, T. Lee, D.F. Davidson, and R.K. Hanson, *UV absorption of CO2 for temperature diagnostics of hydrocarbon combustion applications.* Proceedings of the Combustion Institute, 2005. **30**(1): p. 1591-1599.
93. Neil, M.A.A., R. Juškaitis, and T. Wilson, *Method of obtaining optical sectioning by using structured light in a conventional microscope.* Optics Letters, 1997. **22**(24): p. 1905-1907.
94. Berrocal, E., E. Kristensson, M. Richter, M. Linne, and M. Aldén, *Application of structured illumination for multiple scattering suppression inplanar laser imaging of dense sprays.* Optics Express, 2008. **16**(22): p. 17870-17881.
95. Kristensson, E., *Structured Laser Illumination Planar Imaging SLIPI Applications for Spray Diagnostics*. 2012, PhD Thesis, Lund University.
96. Fernholz, T., H. Teichert, and V. Ebert, *Digital, phase-sensitive detection for in situ diode-laser spectroscopy under rapidly changing transmission conditions.* Applied Physics B, 2002. **75**(2-3): p. 229-236.
97. Tanaka, S., F. Ayala, and J.C. Keck, *A reduced chemical kinetic model for HCCI combustion of primary reference fuels in a rapid compression machine.* Combustion and Flame, 2003. **133**(4): p. 467-481.
98. Christopher, L.H. and T.S. Scott, *Investigation of multi-species (H 2 O 2 and H 2 O) sensing and thermometry in an HCCI engine by wavelength-agile absorption spectroscopy.* Measurement Science and Technology, 2007. **18**(7): p. 1992.
99. Ribarov, L.A., J.A. Wehrmeyer, S. Hu, and R.W. Pitz, *Multiline hydroxyl tagging velocimetry measurements in reacting and nonreacting experimental flows.* Experiments in Fluids, 2004. **37**(1): p. 65-74.
100. Baulch, D.L., R.A. Cox, J.R.F. Hampson, J.A. Kerr, J. Troe, and R.T. Watson, *Evaluated kinetic and photochemical data for atmospheric chemistry.* Journal of Physical and Chemical Reference Data, 1980. **9**(2): p. 295-472.
101. Turns, S.R., *An introduction to Combustion: Concepts and Applications*, ed. 2nd. 2001: The McGraw-Hill Companies.
102. Copeland, C., J. Friedman, and M. Renksizbulut, *Planar temperature imaging using thermally assisted laser induced fluorescence of OH in a methane–air flame.* Experimental Thermal and Fluid Science, 2007. **31**(3): p. 221-236.
103. Chan, C. and J.W. Daily, *Measurement of temperature in flames using laser induced fluorescence spectroscopy of OH.* Applied Optics, 1980. **19**(12): p. 1963-1968.
104. Rensberger, K.J., J.B. Jeffries, R.A. Copeland, K. Kohse-Höinghaus, M.L. Wise, and D.R. Crosley, *Laser-induced fluorescence determination of temperatures in low pressure flames.* Applied Optics, 1989. **28**(17): p. 3556-3566.
105. Atakan, B., J. Heinze, and U.E. Meier, *OH laser-induced fluorescence at high pressures: spectroscopic and two-dimensional measurements exciting the A–X (1,0) transition.* Applied Physics B, 1997. **64**(5): p. 585-591.

106. Kiefer, J., A. Meyerhoefer, T. Seeger, A. Leipertz, Z.S. Li, and M. Aldén, *OH-thermometry using laser polarization spectroscopy and laser-induced fluorescence spectroscopy in the OH A-X (1,0) band.* Journal of Raman Spectroscopy, 2009. **40**(7): p. 828-835.
107. Lucht, R.P., N.M. Laurendeau, and D.W. Sweeney, *Temperature measurement by two-line laser-saturated OH fluorescence in flames.* Applied Optics, 1982. **21**(20): p. 3729-3735.
108. Cattolica, R., *OH rotational temperature from two-line laser-excited fluorescence.* Applied Optics, 1981. **20**(7): p. 1156-1166.
109. Seitzman, J.M., R.K. Hanson, P.A. DeBarber, and C.F. Hess, *Application of quantitative two-line OH planar laser-induced fluorescence for temporally resolved planar thermometry in reacting flows.* Applied Optics, 1994. **33**(18): p. 4000-4012.
110. Giezendanner-Thoben, R., U. Meier, W. Meier, and M. Aigner, *Phase-Locked Temperature Measurements by Two-Line OH PLIF Thermometry of a Self-Excited Combustion Instability in a Gas Turbine Model Combustor.* Flow, Turbulence and Combustion, 2005. **75**(1-4): p. 317-333.
111. Crosley, D.R. and G.P. Smith, *Vibrational energy transfer in laser-excited A2?+ OH as a flame thermometer.* Applied Optics, 1980. **19**(4): p. 517-520.
112. Meier, U.E., D. Wolff-Gaßmann, and W. Stricker, *LIF imaging and 2D temperature mapping in a model combustor at elevated pressure.* Aerospace Science and Technology, 2000. **4**(6): p. 403-414.
113. Agronskaia, A., L. Tertoolen, and H. Gerritsen, *High frame rate fluorescence lifetime imaging.* Journal of Physics D-Applied Physics, 2003. **36**(14): p. 1655-1662.
114. Jacobs, A., M. Wahl, R. Weller, and J. Wolfrum, *Rotational distribution of nascent OH radicals after H2O2 photolysis at 193 nm.* Applied Physics B, 1987. **42**(3): p. 173-179.
115. Baulch, D.L., R.A. Cox, R.F. Hampson, J.A. Kerr, J. Troe, and R.T. Watson, *Evaluated kinetic and photochemical data for atmospheric chemistry.* Journal of Physical and Chemical Reference Data, 1980. **9**(2): p. 295-472.

Summary of papers

I. In this paper, one-dimensional resolved fluorescence lifetimes of two species (CO and OH) are for the first time measured simultaneously in laminar premixed methane/air flames. The measurements are performed with a dual OPG/OPA picosecond laser system together with a streak camera. The measured one-dimensional lifetime profiles at four stoichiometric mixtures (0.9, 1.0, 1.15 and 1.25) generally agree well with lifetimes calculated from quenching cross sections found in the literature and quencher concentrations predicted by the GRI 3.0 mechanism. For OH there is a systematic deviation of approximately 30% between calculated and measured lifetimes. It is found that this mainly is due to the adiabatic assumption regarding the flame and underestimated H_2O quenching cross section in the product zone. Finally, the paper demonstrates the potential for single-shot lifetimes in turbulent situations.

I planned the measurements together with Joakim Bood. I was responsible for building the setup and conducting the measurements. I performed the experimental validation with help from Andreas Ehn and Joakim. Moah Christensen performed the CHEMKIN calculations. I wrote the paper together with Joakim.

II. In this paper, fluorescence lifetimes of toluene are mapped as a function of oxygen concentration in toluene/nitrogen/oxygen-gas mixtures under atmospheric pressure and room temperature conditions using picosecond laser excitation. The data fulfill the Stern-Volmer relation and gives an updated value of the Stern-Volmer slope. Finally, oxygen concentration imaging is performed using a concept termed Dual Imaging with Model Evaluation (DIME).

Andreas Ehn was responsible for planning and conducting the measurements, the data evaluation and writing the paper. I took part in the experimental work regarding the DIME measurements and the final discussion of the results and manuscript.

III. In this paper an 80-picosecond laser pulses of 266-nm wavelength with intensities up to $(2.0 \pm 0.5)\cdot 10^{11}$ W/cm^2 are used for fragmentation of methane/air gas mixtures at ambient pressure and temperature. Emission

spectra are, for the first time, studied with ultrahigh temporal resolution using a streak camera. Fluorescence spectra from CH(A,B,C-X), CN(B-X, Δv = 0, ±1), NH(A-X), OH(A-X) and N_2^+(B-X) are recorded and analyzed. By fitting simulated spectra to high-resolution experimental spectra, rotational and vibrational temperatures are estimated, showing that CH(C), CN(B), NH(A), and OH(A) are formed in highly excited vibrational and rotational states. The fluorescence signal dependencies on laser-intensity and CH_4/air equivalence ratio are investigated as well as the fluorescence lifetimes. These studies suggest that CH(A,B,C) might be formed through neutral dissociation via a super-excited state of CH_4, reached by 3-photon excitation, and that 2-photon ionization/dissociation, rather than collisional quenching, dominates the deactivation of these fragments. All fragments observed are formed within 200 ps after the arrival of the laser pulse and their fluorescence lifetimes are shorter than 1 ns, except for CN(B-X) Δv = 0 whose lifetime is 2.0 ns. The CN(B-X) Δv = 0 fluorescence is studied temporally under high spectral resolution and it was found that the vibrational levels are not populated simultaneously, but with a rate that decreases with increasing vibrational quantum number. Finally, equivalence ratios are determined from "unknown" spectra using multivariate analysis, showing a good agreement with theoretical compositions with an error of 4 %.

I planned the experiments together with Jesper Borggren and Joakim Bood, and was main responsible for conducing the measurements. Jesper, Joakim and I evaluated the data, while Jesper performed the multivariate analysis. I wrote the paper together with Joakim.

IV. In this paper, two-dimensional visualization with nanosecond photofragmentation laser-induced fluorescence on mainly HO_2 and H_2O_2 in different types of laminar premixed flames are for the first time demonstrated. The interference from naturally occurring OH is subtracted. However, it is found that a very small interfering signal in the reaction zone comes from CH_3O_2, while interfering signal in the product zone arises from photolysis of hot CO_2. Relative HO_2, H_2O_2 and CH_3O_2 concentrations are achieved via comparison of calculated concentration profiles obtained in CHEMKIN-II with the Konnov detailed mechanism.

Olof Johansson, Andreas Ehn, Bo Li and Joakim Bood performed the experimental work. Alexander Konnov made the chemical kinetic calculations. I had a minor part in the later part of the experimental work. Olof, Joakim and Andreas wrote the paper and I was involved in the final discussions regarding the manuscript.

V. In this paper, photofragmentation laser-induced fluorescence is performed based on picosecond laser pulses for detection of mainly HO_2 in a stoichiometric laminar methane/air flame. Excitation spectra of the OH photofragments formed in the reaction zone are recorded for pump-probe delays ranging from 0 to 5 ns. The spectra suggest that the population distribution of the nascent OH fragments is rotationally cold and that it takes on the order of 5 ns for the nascent non-equilibrium rotational distribution to relax into a thermal distribution. The radial OH-fragment distribution is extracted from spectral images recorded at six different pump-probe delays. Photochemical OH production is observed both in the reaction zone and the product zone. Comparison with a kinetic model for OH production suggests that more than 60% of the oxygen fragments produced in the reaction zone are formed in the excited ^1D state, explaining a very rapid initial signal growth. The OH-production model is also compared with previous reaction-zone data, acquired with nanosecond laser pulses in the same flame, indicating that no $O(^1D)$, but only $O(^3P)$, is formed. A plausible explanation of the discrepancy between the two results is that the picosecond pulses, having more than two-orders of magnitude higher irradiance than the nanosecond pulses used in the previous study, might cause 2-photon photodissociation, allowing production of $O(^1D)$. Furthermore, the photochemical interference in the product zone, stemming from CO_2 photolysis, could be eliminated by using picosecond pulses and a short pump-probe delay time (< 5 ns).

I planned the experiment together with Joakim Bood. I was main responsible for conducting the experimental work in collaboration with Jesper Borggren and Kajsa Larsson. I evaluated the experimental data and Joakim Bood was responsible for the chemical reaction calculations. I wrote the paper together with Joakim.

VI. In this paper, photofragmentation laser-induced fluorescence is for the first time combined with structured illumination. By frequency modulating the pump-pulse, a well-defined spatial frequency is given to the OH photofragments, making them easily recognized in the frequency domain. By using a post-processing routine based on spatial frequency lock-in detection, the OH-photofragment signal is discriminated against the strong overlapping signal from naturally present OH radicals in the flame. This enables single shot capabilities and shows an increase in signal-to-interference ratio of about two orders of magnitude in the demonstrated application.

Kajsa Larsson, Jesper Borrgren and I were responsible for conducting the experimental work and drafting the paper. The final paper was written by all

authors. Jesper, Elias Kristensson and Andreas Ehn performed the data evaluation.

VII. This paper demonstrates how photofragmentation laser-induced fluorescence for the first time is applied in an HCCI engine for two-dimensional imaging of mainly H_2O_2 and one-dimensional quantitative H_2O_2 concentration measurements at different CADs. Crank-angle resolved quantitative H_2O_2 concentrations are achieved via an on-line calibration procedure by introducing a known amount of vaporized H_2O_2 into the engine cylinder. The CAD resolved H_2O_2 profile is compared with H_2O_2 and HO_2 concentration profiles simulated with DARS and they agree well. The comparison shows that the generated PFLIF signal mainly originates from H_2O_2 with a small interference from HO_2 at especially -23 and +2 CAD. Single-shot two-dimensional imaging demonstrates how H_2O_2 cycle-to-cycle variations can be studied.

Bo Li, Martin Algotsson, Zhongshan Li, Joakim Bood and I planned the measurements. Bo and I were responsible for the experimental setup regarding the lasers, while Martin was responsible for the engine. Bo, Martin and I performed the measurements. Martin did the DARS simulation while Bo was responsible for the experimental evaluations. Bo was main responsible for writing the paper, with assistance by me and Joakim.

VIII. In this paper, a novel approach to evaluate photofragmentation laser-induced fluorescence imaging data is demonstrated to gain experimental quantitative information on the temporal in-cylinder distribution of H_2O_2 in a HCCI. The results from PFLIF are compared to those obtained from chemical kinetics simulations using computational fluid dynamics (CFD) and a stochastic reactor model (SRM). The simulations provide detailed information on the spatial distribution of H_2O_2, HO_2 as well as other important species and temperature. Two-dimensional mass fraction images from PFLIF and CFD show a fair temporal agreement, while details of the spatial distributions disagree. By using probability density functions (PDFs) of H_2O_2 and HO_2 mass fractions, comparisons are made between experimental data and both the CFD and SRM simulations. In general the range of mass fractions show good agreement but the experimental distributions are wider. Possible reasons for this discrepancy are actual heterogeneities in the H_2O_2/HO_2 concentration distributions not predicted by the model, spatial temperature variations, which will influence the strength of the PFLIF signal, spatial variations in the laser profiles, not accounted for in the data processing, and photon noise.

Bo Li and I were responsible for the experimental setup regarding the lasers, while Martin Algotsson was responsible for the engine. I performed the experimental evaluation while Gökhan Coskun did the chemical kinetics simulations and the probability density functions. Gökhan, Joakim Bood, Martin Tunér and I wrote the paper together.

IX. In this paper, the possibility of using photofragmentation laser-induced fluorescence for two-dimensional thermometry in different reacting flows is investigated. OH fragments are created via photofragmentation of H_2O_2 and HO_2 and detected with laser-induced fluorescence. The temperature is determined by fitting simulated OH-excitation spectra of different temperatures to the experimentally recorded spectrum. The method is demonstrated in three different situations, namely a free flow of vaporized H_2O_2 at room temperature, a preheated mixture of $CH_4/N_2/O_2/O_3$ at intermediate temperatures (300-600 K), and in an HCCI engine prior to ignition, i.e. at elevated pressures and temperatures. It is found that the technique performs well in all three cases, with measured temperatures in good agreement with thermocouple readings, for the two first cases, and with temperature calculated based on an isentropic relation for adiabatic compression using measured pressure traces as input for the engine measurements. The temperature maps acquired in the engine experiments reveal inhomogeneous temperature distributions, clearly illustrating the capacity of the technique to yield crucial experimental input to engine modelers and designers.

Elin Malmqvist and I planned the experimental work and conducted the laboratory experiments, whereas I performed the engine experiments. Elin evaluated the experimental data. Elin and I wrote the paper with input from Joakim Bood.